



THE UNIVERSITY of EDINBURGH  
School of Physics  
and Astronomy

# On the characterisation of carbon fibre based electrodes for neural recording

Physics with Year Abroad Project Report

**Harrison F. Squires**

December 27, 2025

## Abstract

This report evaluates the effectiveness of bench-top characterisation of Carbon Cybernetics (CC) Micro Electrode Arrays (MEAs) for neural recording. Electrochemical Impedance Spectroscopy (EIS), commonly used to quantify recording quality, was shown to be a poor predictor of *in vivo* recording fidelity. To address this, a bench-top recording system was developed with the aim of predicting *in vivo* signal quality. In practice, it proved useful only for screening functional and non-functional electrodes. Bench-top SNR also failed to show any predictive value for *in vivo* recording quality. Additional modifications to the recording system allowed testing of spatial selectivity and cross-talk between adjacent channels. Re-analysis of *in vivo* datasets across multiple species revealed that biological variables, rather than impedance or bench-top SNR, play a dominant role in determining recording yield. Finally, a simple probabilistic model based on *in vivo* data, was presented to explore how neuron density may influence the probability of signal detection across species.

Placement Supervisor: Professor S. Prawer

Edinburgh Advisor: Dr. D. Fairhurst

# Personal Statement

I arrived in Melbourne, Australia on July 17<sup>th</sup>, 2024 and met with my local supervisor (Steven) the following day. I began by building a CNC machine and spent the first two weeks learning the basics of G-code and how to mill graphite. In August I began self-teaching an introductory condensed matter course - which I thought might be useful for the project (it turned out not to be). I also started reading literature on topics that I thought might be relevant. However, we soon realised that the initial project (*Diamond Microneedles for Minimally Invasive Blood Collection*) wasn't well suited for a Master's student, as there wasn't much active work to contribute to. It wasn't until the end of August / start of September that we agreed on a new project: the characterisation of Carbon Cybernetics (CC) Microelectrode Arrays (MEAs). The proposed aim was to develop a recording system to characterise these MEAs.

I started September by researching parts needed for a recording system and figuring out how I would obtain recordings. These were ordered, and I began assembling the set-up around mid-September. During this period, I was also consistently reading literature to understand the field and ultimately in preparation for my literature review. From October I started trying to obtain recordings from MEAs and figuring out what variables would be useful to measure to effectively characterise electrodes based on literature and otherwise. From October to December, results were extremely sparse and I struggled to get any meaningful data. I did however, gain familiarity with electrochemical methods and fabrication methods.

From November, I spent evenings working in the College's academic centre writing my Literature review. I continued doing this in my own time until December 17<sup>th</sup>, when I started my Christmas my break. I focused on writing over Christmas whilst travelling around Victoria with my Dad. In the process of writing the literature review the stress of not having meaningful results and the impending deadline started taking a toll on me mentally and I started becoming ill. The literature review was submitted for the deadline and I returned to the lab on January 21<sup>st</sup>.

I wanted to improve my project so I drew up a plan based on my literature review and enacted this in January and February. I increased my working hours and was consistently in the lab from 7:30am to past 5pm, often doing work in the evenings after dinner and weekends. Unfortunately, this along with the stress from the literature review made me more ill and I sought pastoral<sup>1</sup> and medical support and by mid-March was feeling much better!

March, April and May were spent taken experimental measurements and lots of data analysis. The project shifted slightly in scope during this period to focus more on assessing *in vivo* data and understanding flaws in the initial motivation. I began writing this report in April, again in my own time, and it slowly started to take more of a focus from mid-May when experimental work slowed. I remained in Melbourne until June 8<sup>th</sup>, when I returned home, spending June finishing off my report. I intend to spend the first week of July preparing for my final presentation..

---

<sup>1</sup>Especially Dr Mitch Robertson, Dean of Studies at Newman College, for his excellent support and guidance.

# Contents

<b>Acronyms</b>	<b>ii</b>
<b>1 Background &amp; Introduction</b>	<b>1</b>
<b>2 Methods</b>	<b>4</b>
2.1 Electrochemical Impedance Spectroscopy . . . . .	4
2.2 Bench-top Recording system . . . . .	6
2.2.1 SNR analysis . . . . .	7
2.2.2 Fabrication of the stimulating electrode . . . . .	9
2.2.3 3D-Printed Electrode Holder . . . . .	10
2.3 Use of a quasi-point source to determine spatial selectivity . . . . .	13
<b>3 Results &amp; Discussion</b>	<b>14</b>
3.1 Electrochemical Impedance Spectroscopy (EIS) . . . . .	14
3.2 Recording System . . . . .	18
3.2.1 Oscilloscope . . . . .	18
3.2.2 Ripple Grapevine System and Spatial Selectivity . . . . .	21
3.2.3 Dependence of stimulating electrode . . . . .	25
3.3 Understanding the limits of bench-top testing . . . . .	27
3.3.1 Limitations to the experimental methodology . . . . .	27
3.3.2 Re-analysis of <i>in vivo</i> data . . . . .	29
3.3.3 Towards a Computational model based on <i>in vivo</i> data . . . . .	30
<b>4 Conclusions</b>	<b>34</b>
<b>References</b>	<b>41</b>
<b>Appendices</b>	<b>42</b>
<b>A Supplementary Figures</b>	<b>42</b>

# 1 Background & Introduction

Neuroimplantable devices that can connect directly to the brain offer a myriad of possibilities to solve a wide range of health problems. Successful neuroimplantables include devices used to address hearing loss, such as cochlear implants [1, 2]. They also include technologies developed to better understand the brain and to predict or treat diseases such as Parkinson’s disease, epilepsy, and paralysis, including quadriplegia [3–6]. This is achieved through neural recordings, where voltage transients produced by neuronal activity are measured. Recent developments have made it possible to achieve single-cell resolution [7], primarily through reducing the physical size of electrodes and optimising their material properties [8–11].

Micro Electrode Arrays (MEAs) have been developed in various forms for decades; the most notable example is the Utah array, which has been commercialised by Blackrock. The Utah array consists of 100 electrodes arranged in the *xy*-plane with one electrode located at the tip of each shank, as shown in Figure 1a [12]. However, MEAs have been assembled in other configurations, a common alternative being the single-shank design, in which multiple recording sites are distributed linearly along the length of a single probe (Fig. 1b). Silicon-based electrodes are the most popular, which is the case for both Neuronexus (planar) and Utah (3D) arrays [12–15], this is because of the ease of standardisation and reproducible techniques that have been borrowed from microelectronics fabrication [16]. However, as these silicon shanks are rigid they produce scarring in the brain which results in poor performance of the MEA long term [16, 17]; thus, researchers are also trying to implement novel materials in order to improve the performance of the implants and reduce scarring. Alternative materials currently being investigated include carbon-based electrodes, due to their superior flexibility and biocompatibility [11, 17–19]. However, carbon-based electrodes still face challenges with respect to manufacturing at large scales. As new materials and fabrication techniques are introduced in the field, it is essential that these MEAs are fully characterised to understand the impact from the changes compared to state of the art devices and ultimately construct better MEAs.

Carbon Cybernetics (CC) is a Melbourne-based start-up company working to develop carbon-fibre-based electrodes for intracortical neural recording [18, 21]. These are 3D probes with approximately 20 Carbon-fibre electrodes mounted to a Polycrystalline Diamond (PCD), with a pitch varying from 100  $\mu\text{m}$  to 500  $\mu\text{m}$ . Figure 2a shows an Scanning Electron Microscopy (SEM) image of the CC MEA, with fibres spaced 500  $\mu\text{m}$  apart, and Figure 2b shows a close-up SEM image of the carbon fibre. The dark part of the fibre represents the de-insulated, Poly(3,4-ethylenedioxythiophene) (PEDOT)-coated region of the electrode. This appears dark under SEM because it is conductive, and charge is not stored at the surface. The lighter bulk region represents the insulated, Parylene-coated carbon fibre. Parylene is an insulating polymer that is used to control the size of the recording site of an electrode [22].

Characterisation methods currently used in the field have a limited ability to predict electrode performance or to fully understand how changes in electrode parameters affect recording yield and fidelity. Typically an electrode’s impedance (Eq. 1) is used to quantify its performance.

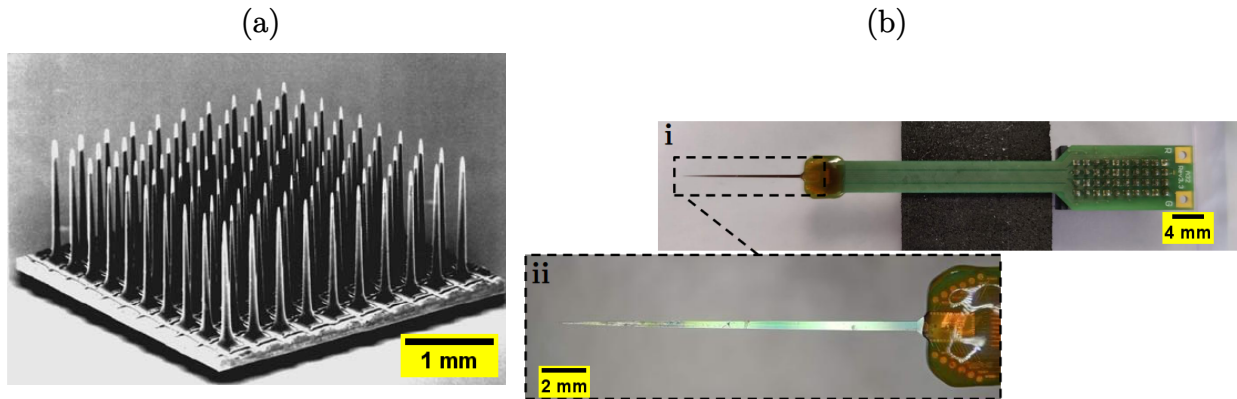


Figure 1. (a) SEM image of a Utah array. 100 fibres mounted to a  $4.2\text{ mm}^2$  grid, pitch of  $400\text{ }\mu\text{m}$ . Scale bar: 1 mm. Image adapted from Kim *et al.* [20]. (b) Photograph of a commercial Neuronexus electrode array (A32; single-shank) mounted on foam, shown at two levels of magnification: (b.i) overview of the full array; (b.ii) zoomed-in view of the electrode tip. While individual electrodes are not clearly distinguishable in the image, 32 planar electrodes are located at the end of the shank. Scale bars: (b.i) 4 mm; (b.ii) 2 mm.

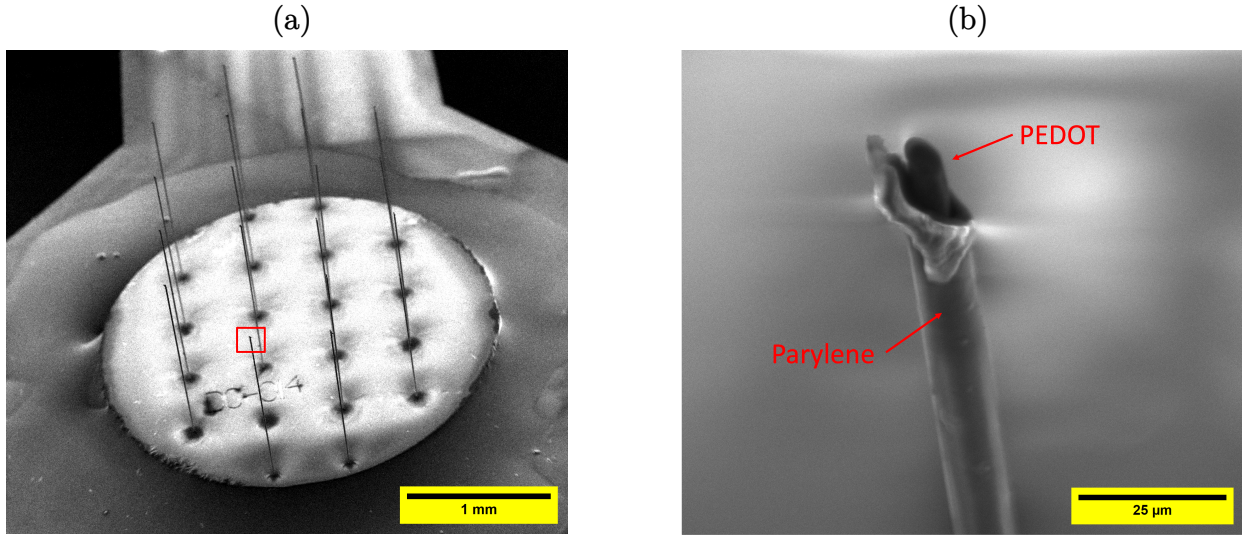


Figure 2. (a) SEM image of a CC MEA, showing 19 fibres arranged on the PCD. Scale bar: 1 mm; Magnification: 39 $\times$ . (b) Close-up of a single fibre, taken from the region indicated by the red box in (a). Fibre has been laser de-insulated, the dark region indicates exposed PEDOT and the lighter gray region is the insulative Parylene-C. Scale bar: 25  $\mu\text{m}$ ; Magnification: 1600 $\times$ .

Impedance characterises an electrode's ability to resist current flow [15, 23].

$$Z(\omega) = \frac{V(\omega)}{I(\omega)} \quad (1)$$

where  $Z$  is the impedance,  $\omega$  is the angular frequency of the signal,  $V(\omega)$  is the potential difference between the working and counter electrodes, and  $I(\omega)$  is the current through the solution.

Impedance at 1 kHz is the most commonly adopted metric to sort electrodes into those expected to perform well or poorly *in vivo* throughout the literature [10, 11, 13–15, 18, 23–27]. Its convenience and widespread implementation have made it the obvious choice for the group thus far. The use of impedance as the defining metric for assessing electrode recording quality is based on its assumed relationship with Signal-to-Noise Ratio (SNR) [11, 15, 18, 24–27]. Specifically, it has been reported that an optimal impedance exists for achieving high SNR. If the impedance is too high, signals may fail to be detected; however, if it is too low, there may be insufficient discrimination between noise and signal, resulting in a low SNR.

That being said, this relationship is heavily disputed [10, 13, 14, 23]. In practice, impedance has proven to be, at best, an inconsistent predictor of recording performance. Therefore, relying on impedance alone is insufficient for confidently optimising for high SNR. Specifically, electrodes with promising impedance at 1 kHz fail to detect signals *in vivo*, while others with similar impedance succeed. As such, it is difficult to confidently discriminate between electrodes using impedance testing alone. Throughout this report, the use of impedance is examined in greater detail together with other techniques to further predict the performance of the electrode. Furthermore, biological variability is studied as a potential root cause of the inability of impedance to fully predict electrode performance *in vivo*.

Screening MEAs prior to *in vivo* insertion is essential for companies like CC, which operate in the neuroimplantable space. MEAs are expensive to produce, both financially and temporally. Moreover, their implantation requires extensive ethical approval [28, 29], and there is a general global trend toward reducing animal testing. As such, confidence in the individual device being implanted is necessary to conserve resources. The testing protocol must therefore be non-destructive and compatible with the fabrication process.

The following report explores the characterisation of CC MEAs. The scope of the project was to improve the reliability of testing methods adopted by the group, which are inconsistent, by the development of a bench-top<sup>2</sup> recording system that can be used to obtain reliable and highly consistent results on an MEAs performance. The data from the bench-top recording system, together with Electrochemical Impedance Spectroscopy (EIS), has been examined to improve the characterisation of CC MEAs prior to implantation. In this context, the broad aim of the project is to use the testing protocol as a quality control measure to predict, with a reasonable degree of certainty, whether an individual electrode can pick up neural signals *in vivo*. At the very least, the aim of the project was to be able to identify electrodes

---

<sup>2</sup>The term bench-top is used here, as *in vitro* is typically reserved for situations involving biological material. Although this is not an explicit requirement by definition, it is the convention adopted throughout the literature.

which are not functional so that they can be excluded from use when the MEA is inserted into brain tissue. This latter aim was fully achieved; accomplishment of the former aim is complicated by the realisation that for electrodes of the size used in this MEA, even if the electrode is fully functional, the probability that it will detect neural signals *in vivo* depends on neural structure, local density of neurons, and other surgical and biological parameters, factors which cannot be predicted by bench-top measurements alone.

These points will be explained in full throughout this report. The first section assesses the predictive value of bench-top characterisation methods, including EIS and bench-top recording. It then examines *in vivo* datasets to identify biological, experimental, and surgical factors that may explain discrepancies between bench-top and *in vivo* measures.

## 2 Methods

### 2.1 Electrochemical Impedance Spectroscopy

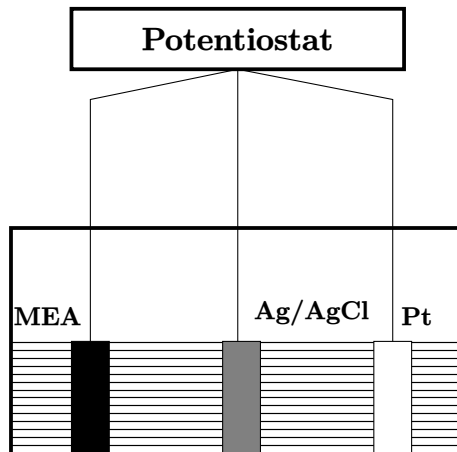


Figure 3. Schematic of the electrochemical setup showing the electrode configuration connected to a potentiostat. This is a three-electrode setup, where the MEA serves as the working electrode, Ag/AgCl as the reference electrode, and Pt as the counter electrode. The horizontal lines represent 0.15 M (physiological) saline. Set-up is used to obtain EIS and capacitance of an electrode. Schematic based on Cui *et al.* [30].

EIS was measured using a three electrode set-up (Fig. 3). An Ag/AgCl electrode (eDAQ; ET054-1 Ag/AgCl Refillable Reference Electrode<sup>3</sup>) served as the reference. To ensure internal consistency, the same reference electrode was used throughout all measurements. A large platinum electrode (eDAQ, ET078-1 70 mm Auxiliary Electrode<sup>4</sup>) was used as the counter electrode [25]. The electrolyte was 0.15 M physiological saline [31]. It was prepared by dissolving NaCl (Sigma-Aldrich, ACS reagent  $\geq 99.0\%$  Purity<sup>5</sup>) in MilliQ water to obtain

<sup>3</sup><https://www.edaq.com/ET054-1>

<sup>4</sup><https://www.edaq.com/ET078-1>

<sup>5</sup><https://www.sigmaldrich.com/AU/en/product/sigald/s9888>

the desired concentration. Saline is the dominant solutions used throughout the literature for bench-top testing due to its similar ionic concentration to *in vivo* conditions [32]. All impedance measurements were performed using a potentiostat (Gamry; Interface 1010E<sup>6</sup>) controlled via the Gamry Framework software [33]. A 10 mV sinusoidal signal was applied over a frequency range from 2 Hz to 200 kHz, and the resulting current was measured to determine changes in impedance magnitude (Eq. 1).

Data was analysed in Python with a custom-made code<sup>7</sup>, based on a script originally implemented by the group. It was expanded to enable full automation and to record values in a spreadsheet for the reported 15 Hz and 1 kHz impedance magnitudes for each channel. These frequencies were selected based on literature suggesting they may serve as key bench-top indicators of *in vivo* performance [15, 26].

In addition, a simplex-optimised least-squares fit was used within the Gamry software. An equivalent circuit model, the Randles circuit (Fig. 4), was also employed. Together, these were used to estimate the double-layer capacitance,  $C_{dl}$ , of the electrode-electrolyte interface [34–37]. MEAs and stimulating electrodes were characterised using this approach.

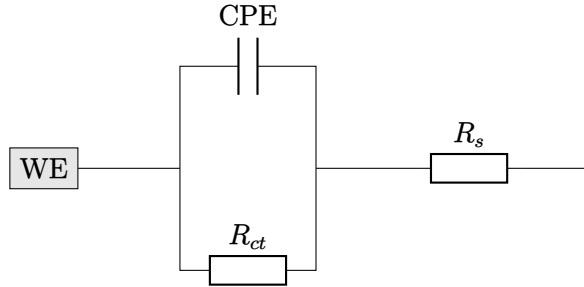


Figure 4. Circuit diagram of the Randles circuit, the typical equivalent circuit model used to determine the capacitance from an EIS spectrum. Here, **WE** denotes the working electrode. Circuit diagram based on Shen *et al.* [34], Wang *et al.* [35], Lazanas and Prodromidis [36]

$$Z_{\text{tot}}(\omega) = R_s + \frac{1}{\frac{1}{R_{ct}} + (i\omega)^{\alpha} Q} \quad (2)$$

where  $Z_{\text{tot}}(\omega)$  is the total impedance,  $R_s$  is the series resistance (i.e., the solution resistance),  $R_{ct}$  is the charge transfer resistance,  $Q$  is the pseudocapacitance of the solution, and  $\alpha$  is the Constant Phase Element (CPE) exponent, with  $\alpha \in (0, 1]$ .

CPE is used in the description of imperfect capacitors, such as the double-layer capacitance,  $C_{dl}$  [37]. If the system acts purely capacitively, then  $\alpha = 1$ . This implies  $Q = C_{dl}$ . However, in real systems where  $\alpha \neq 1$ , the effective capacitance can be estimated using Brug's formula [38]:

$$C_{dl} = Q^{\frac{1}{\alpha}} \cdot \left( \frac{1}{R_s} \right)^{\frac{1-\alpha}{\alpha}} \quad (3)$$

<sup>6</sup><https://www.gamry.com/potentiostats/interface/interface-1010e-potentiostat/>

<sup>7</sup>Available in the appendix

This expression assumes that the capacitance is frequency-independent, which is an approximation valid when reactions are assumed to be non-faradaic<sup>8</sup> [38].

$Q$  and  $\alpha$  were determined by minimising the least-squares error between the measured and modelled EIS,

$$\min_{R_s, R_{ct}, Q, \alpha} \sum_{\omega} |Z_{\text{measured}}(\omega) - Z_{\text{model}}(\omega; R_s, R_{ct}, Q, \alpha)|^2 \quad (4)$$

where a value of  $0.7 < \alpha \leq 1$  is assumed appropriate for estimating  $C_{dl}$ .

## 2.2 Bench-top Recording system

A custom bench-top system was developed to assess the recording performance of CC MEAs under controlled, non-biological conditions in 0.15 M saline. The system was used to evaluate each channel's ability to detect externally applied stimuli prior to implantation, and to assess whether bench-top SNR could be predictive of *in vivo* recording fidelity [24, 39]. All procedures were designed to be fully non-destructive to preserve the MEA for subsequent *in vivo* use.

The MEA was placed in a custom-designed 3D printed saline bath (§ 2.2.3). This ensured fixed positioning of the MEA for consistent results. An Ag/AgCl electrode (eDAQ; ET054-1 Ag/AgCl Refillable Reference Electrode<sup>9</sup>) was used as the reference electrode. This choice was motivated by its low susceptibility to polarisation and its high compatibility with 0.15 M saline [31, 40, 41]. 0.15 M saline, consistent with that used in EIS, was prepared as previously described (§ 2.1). All stimulation and recording hardware was grounded directly to this reference electrode. A star topology was adopted to minimise ground loops by shorting all grounds to a single point in the system [42]. A schematic of this is shown in Figure 5.

A DAQ (National Instruments; USB 6221 Data Acquisition Device) was used to generate the stimulus pulse. Initially, the same DAQ was used for both stimulation and recording, but this configuration introduced electrical artefacts due to cross-talk<sup>10</sup>. These artefacts manifested as large, false signals that appeared independent of the MEA channel being tested, making it impossible to reliably compare responses across the MEA. To address this, two separate devices were used for stimulation and recording.

A small stimulating electrode, rather than parallel plates [24], was used to generate signals with comparable magnitude and spatial extent to an Action Potential (AP) and was connected directly to the DAQ. It was mounted to a motorised micro-manipulator (Sutter instruments; ROE-200 and MPC-200<sup>11</sup>), allowing micro-metre scale control over the positioning in all three spatial dimensions. This configuration allowed the stimulating electrode to be positioned directly above specific recording channels on the MEA, with the aim of achieving spatial selectivity.

---

<sup>8</sup>That is, no net redox reactions occur at the electrode-electrolyte interface

<sup>9</sup><https://www.edaq.com/ET054-1>

<sup>10</sup>An unwanted transfer of signals between channels.

<sup>11</sup>[https://www.sutter.com/MICROMANIPULATION/mpc325\\_frame.html](https://www.sutter.com/MICROMANIPULATION/mpc325_frame.html)

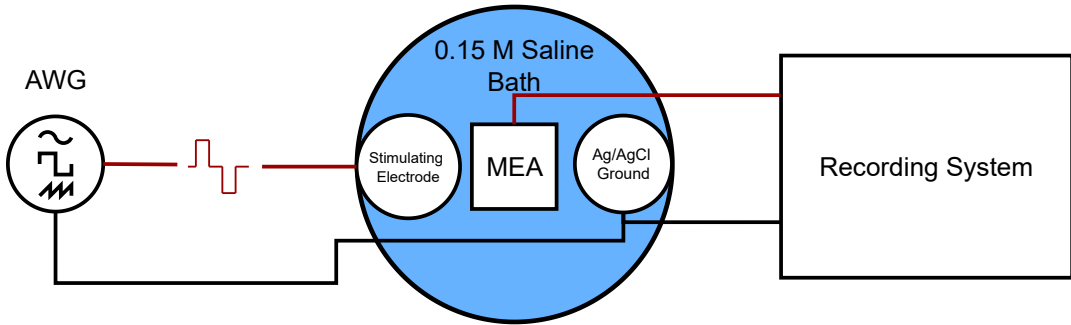


Figure 5. Schematic of the stimulation and recording configuration used in this study. A waveform generator (AWG) produces a biphasic stimulus, which is delivered via a stimulating electrode positioned above the MEA, indicated by the red lines. The stimulating electrode is mounted to a micro-manipulator for precise control. The MEA is immersed in a 0.15 M saline bath alongside an Ag/AgCl reference electrode, which serves as the common ground for both the recording system and the stimulator. All grounds are connected to a single point using a star topology to minimise ground loops, as shown by the black lines.

For recording, two different systems were employed throughout: an Oscilloscope (Pico; Picoscope 2206B<sup>12</sup>) and the Ripple Grapevine System (RGS). Both devices shared the same electrical configuration (Fig. 5). The RGS had the advantage of being able to record up to 32 channels<sup>13</sup> simultaneously, whereas for the oscilloscope only one channel was able to be recorded at once. The RGS incorporates both analogue and digital filtering: the raw analogue signal is passed through a third-order Butterworth filter (0.3 Hz high-pass, 7.5 kHz low-pass) prior to digitisation [43], enabling the detection of microvolt-scale signals<sup>14</sup> both *in vivo* and during bench-top testing. In contrast, the oscilloscope was limited to detecting signals in the millivolt range due to its higher noise floor.

The RGS is a high-cost commercial system (~\$50,000 AUD), whereas the oscilloscope is a low-cost alternative (~\$1,000 AUD). The two systems were compared to determine whether the oscilloscope could provide comparable assessments of MEA functionality during bench-top testing. This would support the use of a low-cost system for pre-implantation testing. The RGS could then be reserved for animal experiments, where its signal processing and multi-channel recording are most essential.

### 2.2.1 SNR analysis

Custom code<sup>15</sup> was written in order to analyse the results from the recording system, using both the oscilloscope and the RGS. The SNR was obtained from the recording system and this was used to quantify the effectiveness of the recording quality of CC MEAs. For the

<sup>12</sup><https://shorturl.at/LX9Qy>

<sup>13</sup>A CC MEA has 20 at most.

<sup>14</sup>The magnitude of an extracellular AP is typically on the order of hundreds of microvolts.

<sup>15</sup>Available upon request

purposes of this report, the following definition was adopted for SNR:

$$\text{SNR} = 20 \log_{10} \left( \frac{\langle V_{\text{PP}}^{\text{signal}} \rangle}{\sigma_{\text{RMS}}^{\text{noise}}} \right) \quad (5)$$

where  $\langle V_{\text{PP}}^{\text{signal}} \rangle$  is the average peak-to-peak voltage of the signal measured by the recording electrode. Peaks were identified using a dynamic threshold, and each recording track was manually inspected to ensure appropriate peak detection.  $\sigma_{\text{RMS}}^{\text{noise}}$  is the standard deviation of the background noise, measured in the absence of stimulation. The factor of 20 ensures that the bench-top SNR is reported in dB, this was chosen to improve visual clarity when plotting.

This is largely in line with SNR calculations performed on the bench-top and *in vivo* throughout the literature [24, 44]. However, some studies report linear SNR values [44], given by

$$\text{SNR} = \frac{\langle V_{\text{PP}}^{\text{signal}} \rangle}{\sigma_{\text{RMS}}^{\text{noise}}}. \quad (6)$$

Linear SNR is reported for *in vivo* measurements, following the lab's protocol. Although the definitions differ, comparisons between bench-top and *in vivo* SNR are limited to qualitative trends rather than a discussion of absolute magnitudes.

Two codes were used to separately analyse the oscilloscope data and the data from RGS. The oscilloscope code was written in MATLAB from scratch. The Ripple code was based on existing code from the lab and was heavily modified for the system discussed here. The calculations performed were consistent across both recording devices. However, filtering was applied only to the Ripple recordings. The oscilloscope data were left unfiltered to provide a closer measure of the electrode's intrinsic performance, without additional filtering from either software or hardware sources.

Uncertainty in the calculated SNR was estimated by propagating error from the peak-to-peak voltage term in Equation 5. Variability in the signal was quantified using the standard deviation of the peak-to-peak voltage across all detected waveforms within a track. Background noise, denoted  $\sigma_{\text{RMS}}^{\text{noise}}$ , was assumed to remain stable over the recording duration, and thus its contribution to uncertainty was neglected in the propagation.

The resulting uncertainty in SNR was calculated using standard error propagation applied to Equation 5:

$$\delta(\text{SNR}) = \frac{20}{\ln 10} \cdot \frac{\delta(\langle V_{\text{PP}}^{\text{signal}} \rangle)}{\langle V_{\text{PP}}^{\text{signal}} \rangle} \quad (7)$$

where  $\delta(\langle V_{\text{PP}}^{\text{signal}} \rangle)$  represents the standard error,  $\frac{\sigma}{\sqrt{n}}$ , of the mean peak-to-peak voltage, calculated as:

$$\delta(\langle V_{\text{PP}}^{\text{signal}} \rangle) = \frac{\sigma_{\text{PP}}^{\text{signal}}}{\sqrt{n}} \quad (8)$$

where  $n$  is the number of detected waveforms per track (typically  $n = 900$ ), and  $\sigma_{\text{PP}}^{\text{signal}}$  is the standard deviation of the peak-to-peak voltages.

## 2.2.2 Fabrication of the stimulating electrode

Custom-made stimulating electrodes were developed to deliver electrical stimuli for the bench-top recording system. The following fabrication protocol describes how the stimulating electrodes were produced. A 75 µm diameter Platinum-Iridium (Pt–Ir) wire (Goodfellow; Platinum/Iridium Alloy Straight Wire, Pt90/Ir10<sup>16</sup>) was soldered to one end of a 200 µm diameter copper wire (Altronics), forming the exposed stimulation tip. Approximately 1000 µm of Pt–Ir was used to ensure mechanical and electrical stability. Stimulating electrodes were fabricated by inserting the copper and platinum wire assembly into a glass capillary tube (Harvard Apparatus; 30-0057; GC150F-10; 1.5 OD x 0.86 IK x 100 L mm<sup>17</sup>), which was pulled to produce a tapered tip of approximately 100 µm. The glass capillary was fabricated using a laser-based micro-pipette puller (Sutter Instruments; Model - P2000<sup>18</sup>). This design ensured the exposed Pt–Ir tip functioned as the stimulation source for the bench-top recording system. Figure 6 shows a completed device. If the internal wire assembly was too large to fit through the capillary tip, the glass opening was enlarged by carefully trimming the ends with a razor blade under a microscope [45].

Selleys Araldite 5 Minute Epoxy<sup>19</sup> was used to secure the assembly and insulate the exposed Pt–Ir wire from the copper conductor contained inside the capillary tube. The epoxy was mixed thoroughly on a microscope slide and applied using the fine end of another pulled glass capillary tube under a microscope. This process allowed precise control of the exposed Pt–Ir tip and ensured both ends of the capillary were sealed. The epoxy was allowed to cure for a minimum of three hours, although electrodes were typically left to cure overnight to ensure robust insulation and a strong mechanical assembly.

After curing, a small length of heat-shrink (RS PRO; Heat Shrink Tubing, black, 3 mm sleeve diameter × 10 m length, 3:1 shrink ratio<sup>20</sup>) tubing was placed over the shaft of the capillary. A gold pin was soldered to the opposing end of the copper wire, relative to the Pt–Ir, to enable connection to external electronics.

The exposed length of Pt–Ir at the tip was measured using a micro-metre slide and trimmed to approximately 150 µm. This step also served to visually assess the integrity of the epoxy seal. If necessary, a second thin layer of epoxy was applied and left to cure overnight to improve the insulation. Each stimulating electrode was also submerged in a saline bath for 30 min to observe whether any saline entered the tube through capillary action. If this occurred, the insulation was deemed insufficient and the electrode was discarded.

Each stimulating electrode was characterised using EIS to confirm electrical connectivity and quantify impedance and capacitance. This was performed in the same way as for CC MEAs, using 0.15 M saline, comparing 15 Hz and 1 kHz impedance magnitudes. This allowed control over variability between electrodes, ensuring that electrode-to-electrode differences were not mistaken for MEA performance.

<sup>16</sup><https://www.goodfellow.com/global/platinum-iridium-alloy-straight-wire-pt90-ir10-group>

<sup>17</sup><https://www.warneronline.com/clark-borosilicate-standard-wall-with-filament>

<sup>18</sup><https://www.sutter.com/MICROPIPETTE/p-2000.html>

<sup>19</sup><https://shorturl.at/YvDCw>

<sup>20</sup><https://shorturl.at/tcSaE>

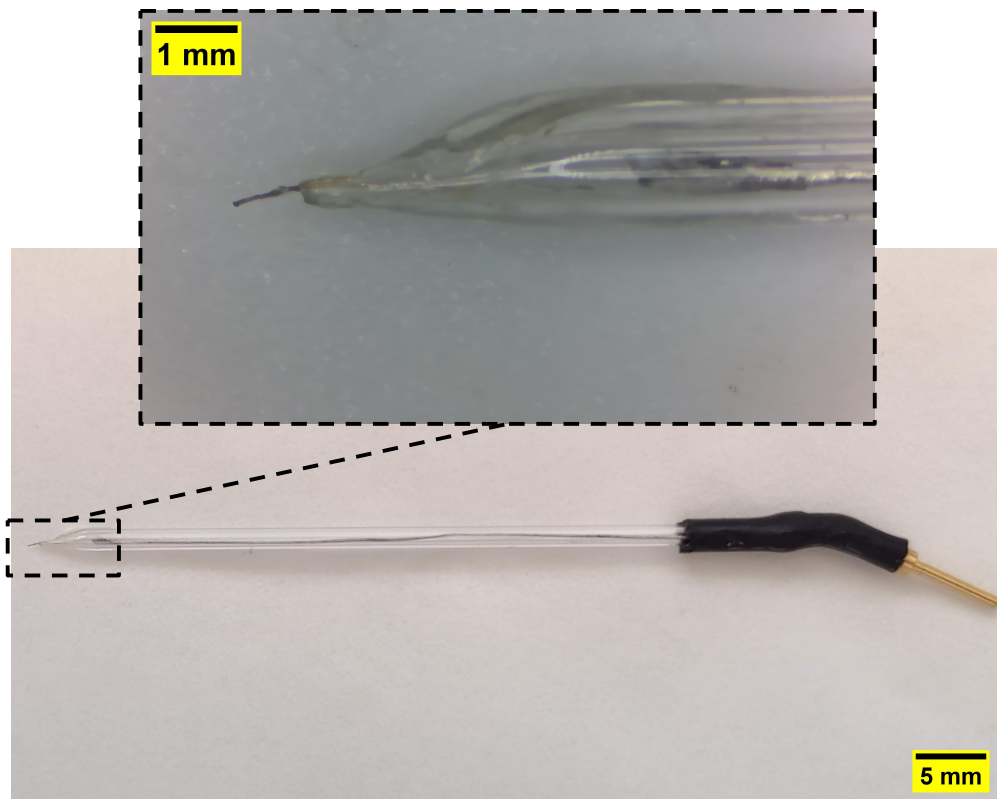


Figure 6. Fabricated stimulating electrode assembled according to the protocol described above. The left end features a Pt–Ir tip enclosed within a pulled glass capillary, while a copper wire runs internally and is insulated with epoxy. The right end terminates in a gold pin for electrical connection, secured with heat-shrink tubing. This device was used to deliver electrical stimulation in saline. Main image scale bar: 5 mm. Inset: magnified view of the exposed Pt–Ir tip before trimming to 150  $\mu\text{m}$ , scale bar: 1 mm.

Following any saline exposure, electrodes were cleaned with ethanol and rinsed with MilliQ water to remove residual saline and prevent build-up between uses. To maintain internal consistency within each MEA recording, the same stimulating electrode was used across all channels in a given MEA. Between different MEAs, different stimulating electrodes were occasionally used; however, care was taken to select electrodes with minimal variation in tip exposure and impedance spectra throughout the investigation. Unless otherwise stated, all results presented in this report were obtained using the custom-made stimulating electrode described above.

### 2.2.3 3D-Printed Electrode Holder

The MEAs used in this study were proprietary; as a result, no commercially available holder exists. To address this, a custom, non-destructive mounting system was developed for bench-top testing. Computer Aided Design (CAD) software (TinkerCAD<sup>21</sup>) was used to create a

<sup>21</sup>[www.tinkercad.com](http://www.tinkercad.com)

two-part saline bath that securely held the MEA during submerged bench-top testing. As shown in Figure 7, CC MEAs include a small plastic component affixed to the back. This stalk was originally designed for *in vivo* insertion using self-closing tweezers. This component is fixed relative to the electrode fibres and was used to ensure repeatable placement of the arrays within the setup by incorporating a mounting hole of matching diameter into the base of the electrode holder.

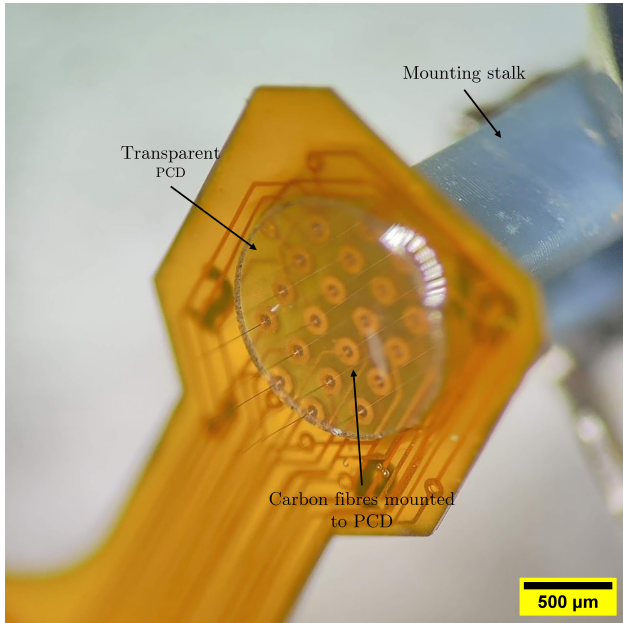


Figure 7. Microscope image of a CC MEA, showing the transparent PCD with carbon fibres mounted onto its surface. The 3D-printed resin mounting stalk is also visible, providing mechanical stability and consistent positioning during experiments. Scale bar: 500  $\mu\text{m}$ .

The electrode holder mounts directly to the microscope stage, as shown in Figure 8a, allowing four degrees of freedom:  $x$ ,  $y$ ,  $z$ , and  $\theta$ . This flexibility ensures accurate positioning of the stimulating electrode across the full travel range of the micromanipulator ( $\sim 25\,000 \mu\text{m}$ ).

In this setup, the mounting stalk secures the electrode within a custom-designed saline bath by press-fitting into the matching hole in the base. Approximately 20 iterations were undertaken to optimise the holder design. Fabrication was carried out using a resin-based 3D printer (Phrozen; Phrozen Sonic Mini 8K S), which was capable of producing water-tight components.

Initially, the design included a base piece with a slot for the stalk and a lid that applied downward pressure on the ribbon cable leading from the MEA. However, this configuration introduced two main problems: the lid was difficult to insert without displacing or damaging the array, and the saline bath often leaked. Application of a silicone elastomer to seal the lid and bath was trialled, but it introduced a tight fit that again risked damage when disassembling the setup.

The revised design fixed the base to the microscope stage. The MEA could then be positioned with the lid gently placed on top, improving both ease of use and reproducibility. Leakage

of the electrolyte was eliminated. Installation of the MEA into the bath was considerably less destructive.

A side-mounted holder was added for the Ag/AgCl reference electrode (Fig. 8) to fix its position relative to the MEA. This improved experimental consistency between recordings. In electrochemical experiments, it is best practice to place the reference electrode farther from the stimulation site than the recording MEA [36]. In this setup, only the stimulating electrode was movable, allowing precise control via a micromanipulator and reducing variability in the recording system.

The final design incorporated two 37 mm O-rings (AIMS; NBR 70 O-Ring Metric 37 × 2 mm<sup>22</sup>) to ensure a watertight seal. Depressed channels matching the O-ring dimensions were included in both the base and lid components to hold them in place, as shown in Figure 8b.

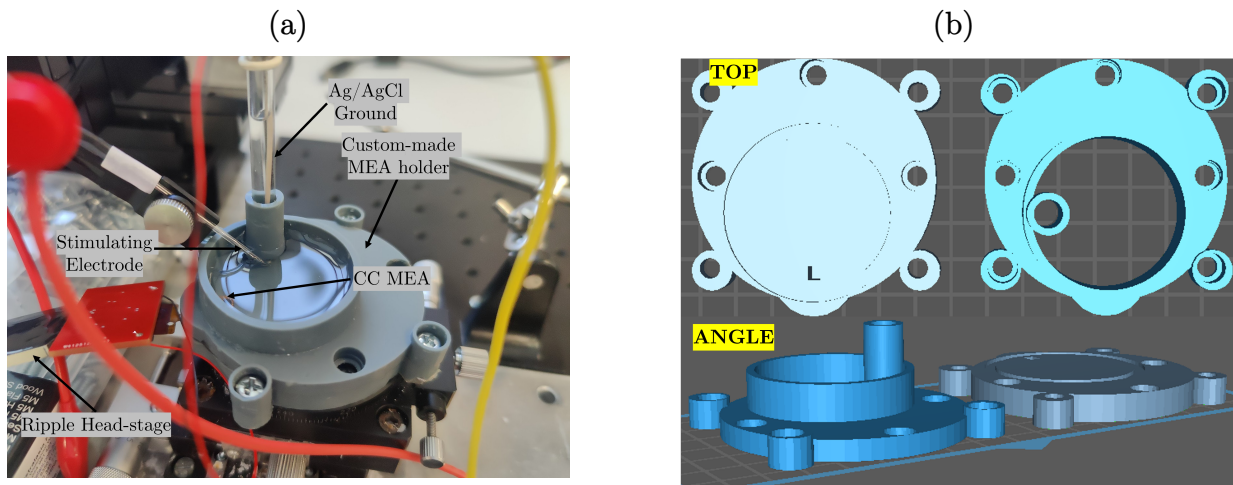


Figure 8. Electrode holder used for the bench-top recording system. The design ensures stable and repeatable recordings by maintaining a sealed saline bath with fixed positioning of the MEA and the AgCl ground. (a) Photograph of the assembled holder during active data acquisition. The CC MEA is seated in the central hole and connected to a red PCB, which interfaces with the RGS via an Omnetics connector. The MEA itself is positioned at the edge of the saline bath; although the array is not clearly visible, the ribbon cable emerging from the red PCB indicates its location. The Ag/AgCl reference electrode is inserted vertically through the side-mounted holder. The bath is filled with 0.15 M saline. (b) 3D model of the custom holder, showing top and angled views. The design incorporates two O-rings (not shown), compressed by applied downforce, to form a water-tight seal and prevent electrolyte leakage. The top holes are used for mounting and sealing via M4 screws (14 mm length).

Two part epoxy was used to affix the O-rings. After thorough mixing, a thin layer of epoxy was applied to the seating area using a needle. Care was taken to avoid coating the

<sup>22</sup>[https://www.aimsindustrial.com.au/nbr-70-o-ring-imperial-37-x-2mm-25-pieces?gad\\_source=1&gclid=CjwKCAjw3P-2BhAEEiwA3yPhwFpkWTqEIbfFm\\_aj4vYuMn0BiLcD50vHVGnHF-ph2cDyDLdPb2\\_7YhoCO2AQAvD\\_BwE](https://www.aimsindustrial.com.au/nbr-70-o-ring-imperial-37-x-2mm-25-pieces?gad_source=1&gclid=CjwKCAjw3P-2BhAEEiwA3yPhwFpkWTqEIbfFm_aj4vYuMn0BiLcD50vHVGnHF-ph2cDyDLdPb2_7YhoCO2AQAvD_BwE)

exposed portions of the O-rings, as this would form a rigid resin layer that prevents proper compression of the O-rings and compromising the water-tight seal. A minimum curing time of 24 hours was used before exposure to saline.

Threaded nuts were embedded in the base piece and secured in place with epoxy, enabling the two components to be screwed together. All screw holes were countersunk to ensure even compression. The downward force from the screws was sufficient to produce a reliable seal. Between uses, the bath was cleaned with MilliQ water.

### 2.3 Use of a quasi-point source to determine spatial selectivity

A glass capillary tube was pulled to a fine tip, producing a patch-clamp electrode with  $\sim 10 \text{ M}\Omega$  impedance [39]. A variable volume single-channel pipette (Eppendorf; Pipette Variable, 1-Channel, 0.5  $\mu\text{L}$  to 10  $\mu\text{L}$ <sup>23</sup>) was used to load 7  $\mu\text{L}$  of 0.15 M physiological saline into each capillary. The patch-clamp electrode was mounted in a patch-clamp holder, with the tip positioned in a saline bath alongside the MEA, and connected to the RGS<sup>24</sup>. The patch-clamp holder was then mounted to a micro-manipulator. A voltage source was delivered through the patch-clamp pipette using an arbitrary waveform generator (Rigol; DG4162 Arbitrary Waveform Generator<sup>25</sup>) for sinusoidal<sup>26</sup> pulses. The National Instruments DAQ was used for biphasic stimulation. Two separate<sup>27</sup> Ag/AgCl grounds were used for the stimulator and the RGS. The set-up used is now the largely similar to Figure 5. This resulted in recorded signals on the order of several hundred microvolts<sup>28</sup> when the stimulating electrode was positioned within 5  $\mu\text{m}$  of the recording site, consistent with the magnitude of an AP.

The RGS was used for recordings and was connected to the MEA via an Omnetics connector (Fig. 8a). To reduce electrical noise, the RGS was wrapped in aluminium foil and grounded to earth, which significantly reduced baseline fluctuations, noise of 14  $\mu\text{V}_{\text{RMS}}$  was consistently achieved.

Once aligned, the patch-clamp electrode was incrementally moved in 10  $\mu\text{m}$  steps to quantify the effects of lateral displacement between an individual channel and the quasi-point source. The patch-clamp pipette effectively models the spatial extent of a neural AP [39].

Next, to assess cross-talk, the patch-clamp electrode was sequentially positioned above each channel on a CC MEA. Figure 9 shows the patch-clamp electrode aligned with one of the fibres of the array. This approach enabled controlled, localised stimulations of an individual channel. Each channel on the array was simultaneously measured; the magnitude of the peak-to-peak voltage was compared relative to the electrode being intentionally stimulated.

<sup>23</sup><https://shorturl.at/JQr8L>

<sup>24</sup>The connection to the recording set-up is the same as described previously.

<sup>25</sup><https://www.batronix.com/shop/waveform-generator/Rigol-DG4162.html>

<sup>26</sup>Sinusoidal pulses were initially used to follow the protocol described by Viswam *et al.* [39].

<sup>27</sup>A dual-ground configuration initially caused instability in the screening-capable recording setup, likely due to mismatched ground electrodes, specifically the use of a large platinum ground alongside a separate recording ground. However, stable performance was achieved by using two Ag/AgCl electrodes for grounding the stimulator and the RGS, consistent with the configuration used by Viswam *et al.* [39].

<sup>28</sup>Because the signals were much smaller than millivolts, the oscilloscope could not be used.

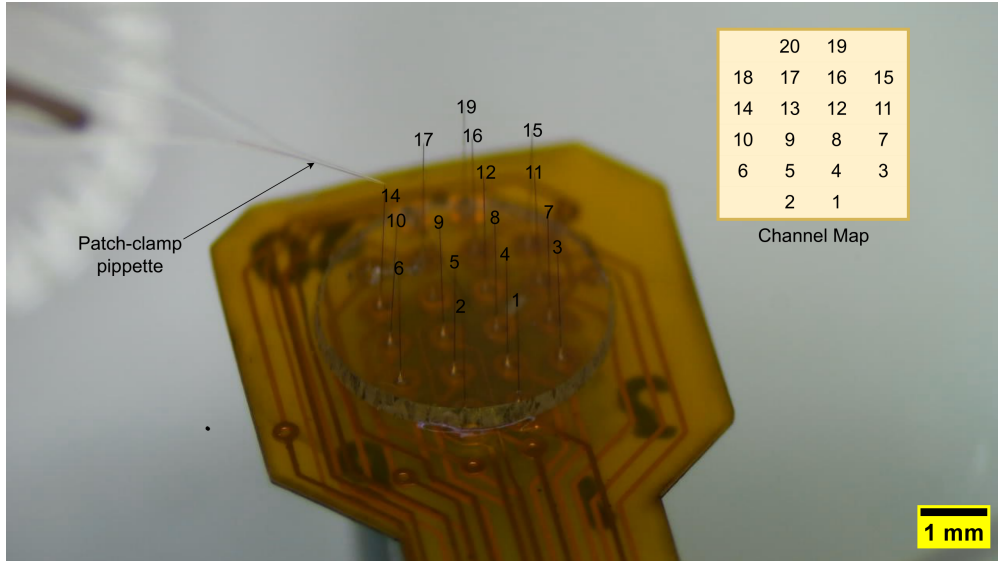


Figure 9. Microscope image showing a patch-clamp electrode tip and a CC MEA optically aligned within approximately the same *xy*-plane. A lateral separation of approximately 1  $\mu\text{m}$  between the patch-clamp tip and Channel 14 is shown. This configuration was used to assess the spatial selectivity of a small quasi-point source (the patch-clamp electrode) relative to the recording MEA. The numbers above the carbon fibres indicate the channel number of the PCB and the channel map on the right side is a tabular format of this. Scale bar: 1 mm

### 3 Results & Discussion

This section presents and discusses the results of bench-top characterisation. It begins by assessing the relationship between EIS and recording fidelity *in vivo*. Subsequently, the relationship between bench-top recordings and *in vivo* measurements is evaluated. Following this, the spatial extent of CC MEAs and methods for assessing cross-talk are discussed. The dependence of recording outcomes on the stimulating electrode is then examined. Next, the limitations of bench-top metrics are explored in the context of biological variability and surgical factors, based on a re-analysis of *in vivo* datasets and reports in the wider literature. Finally, the foundations are laid for a simple probabilistic model to predict the likelihood of a channel measuring neural activity, based on the neuron density of the animal model.

#### 3.1 Electrochemical Impedance Spectroscopy (EIS)

EIS was used during the characterisation of the CC MEAs. Prior to the commencement of this project, EIS had been used exclusively within the group to assess MEA performance before *in vivo* experiments, although quantitative comparisons with *in vivo* data had not been performed. The impedance at 1 kHz is commonly used as an indicator of expected electrode performance *in vivo*. However, the relationship between EIS and *in vivo* MEA performance remains unclear. While some studies support its predictive value [15, 24, 26], others warn against its adoption [10, 13, 14, 23]. As part of the work in this project, the

use of EIS has been continued and expanded by considering other frequencies in addition to the 1 kHz metric. Impedance at lower frequencies, such as 15 Hz have also been explored as potential indicators of recording quality, as suggested primarily by Harris *et al.* [26] and Baranauskas *et al.* [15].

A typical impedance spectrum, as shown in Figure 10, for a CC MEA, shows a clear difference between the spectra of functional and non-functional electrodes. Functional channels exhibit smooth, continuous curves, whereas non-functional channels feature a jagged relationship between  $|Z(f)|$  and  $f$ . This is mostly due to the higher impedance meaning there is an introduction of noise to the potentiostat, reducing the reliability of the data [46].

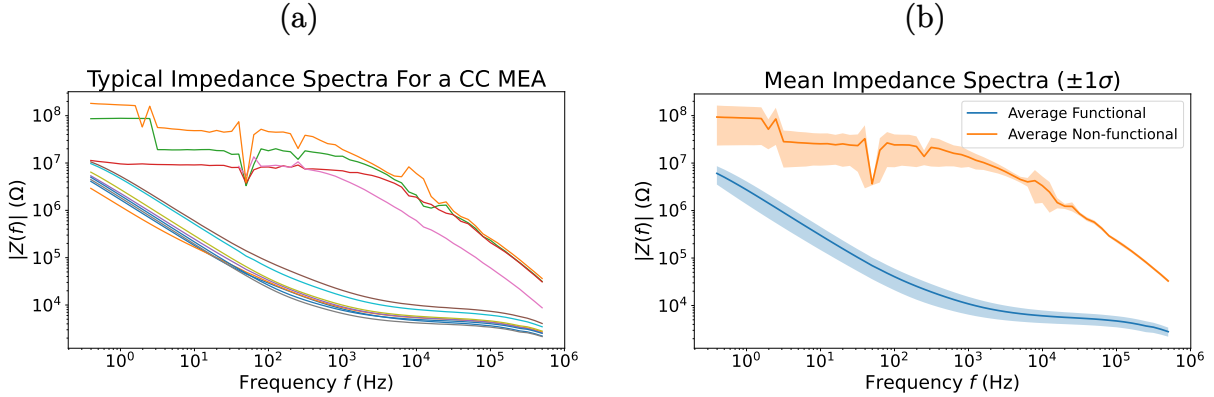


Figure 10. (a) Typical EIS spectra for a CC MEA, showing 8 functional channels and 4 non-functional channels. The channels cluster distinctly into functional and non-functional groups based on their impedance spectra. (b) Averaged impedance spectra for a well-functioning electrode (blue) and a non-functional fibre (orange). The shaded regions represent uncertainty, shown as  $\pm 1\sigma$  from the mean across the 8 functional and 4 non-functional fibres.

For functional channels, two regimes are clearly displayed. At lower frequencies, below approximately  $10 \times 10^3$  Hz, capacitive behaviour is observed, where  $|Z(f_{low})| \propto f$ . At higher frequencies, above approximately  $10 \times 10^4$  Hz, resistive behaviour dominates, where the evolution of  $|Z(f)|$  with respect to  $f$  ceases. In a purely resistive system, we expect  $\frac{d|Z(f)|}{df}$  to vanish, since in the resistive limit,  $|Z| \rightarrow |R|$ , where  $R$  is the resistance at the electrode-electrolyte boundary [36]. Non-functional channels may consist of those without fibres attached, with physically damaged fibres, or with no visibly apparent issue, e.g. a damaged PEDOT coating.

In-line with frequent reports in the literature, the 15 Hz and 1 kHz impedance values for each channel were plotted in Figure 11 for a typical CC MEA, to draw more clear intra-array comparisons. Impedance values at 1 kHz and 15 Hz are reported as per-channel values, without formal uncertainty propagation. However, uncertainty is presented in Figure 10 for functional and non-functional groups, reflecting intra-channel variability. This reflects common practice in the literature for the reporting of individual channel impedance [10, 15, 23]. No discernible trends are evident here, i.e. the use of 15 Hz vs 1 kHz does not

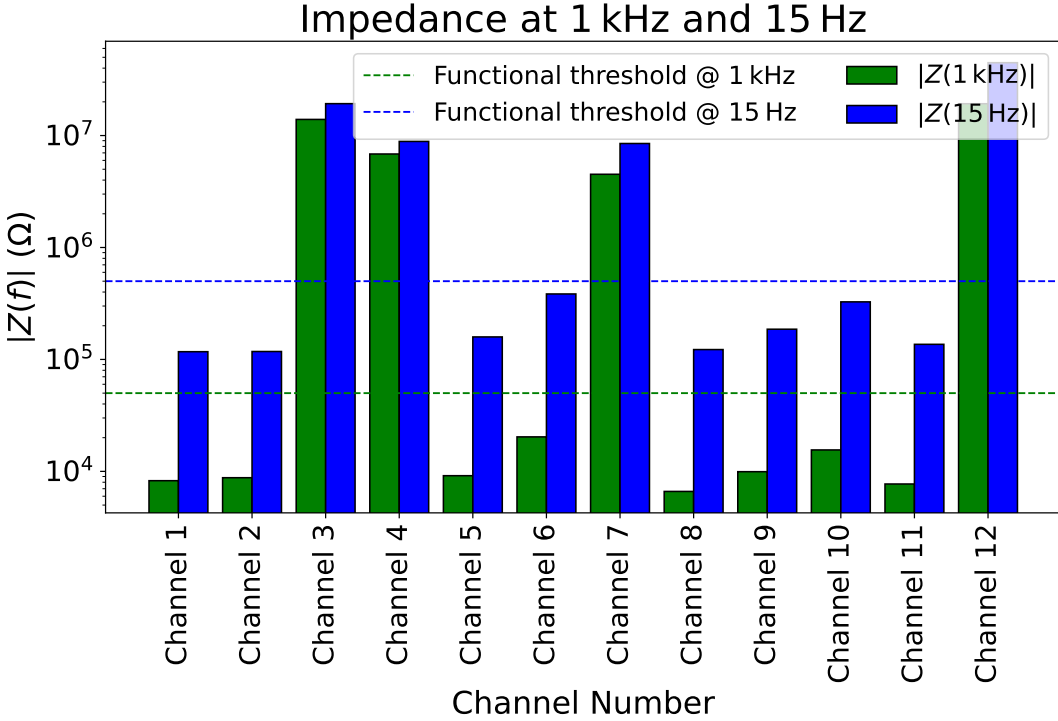


Figure 11. A comparison between 1 kHz impedance (green) and 15 Hz impedance (blue) for a typical CC MEA. Trends are consistent between both reported frequencies. Dashed threshold lines are imposed on the plot at  $5 \times 10^4 \Omega$  and  $5 \times 10^5 \Omega$  respectively. Channels above these thresholds failed to record signals *in vivo* in all instances. Channels 3,4,7,12 are deemed as non-functional.

provide any benefit in sorting electrodes. This suggests that neither frequency offers a clear advantage for predicting electrode performance, despite reports that lower-frequency impedance may better reflect *in vivo* recording fidelity [15, 25]. The deemed functional and non-functional channels are consistent across these frequencies. Channels with an impedance at 1 kHz below  $\sim 10 \times 10^4 \Omega$  and 15 Hz below  $\sim 10 \times 10^5 \Omega$  were deemed as functional. This conclusion was based on the observation that channels exceeding these impedance thresholds consistently failed to record *in vivo* spikes in all instances. Functional channels reported a 1 kHz impedance of  $9.1(60) \times 10^3 \Omega$  and 15 Hz impedance of  $1.2(10) \times 10^4 \Omega$ .

More broadly, while impedance allowed for grouping into functional and non-functional channels, it failed to predict which electrodes would record signals *in vivo*. Even within the functional group, only a subset consistently recorded neural activity. For instance, for an MEA with 8 channels identified as functional (Fig. 10), only 4 successfully recorded signals across two separate insertions. This observation is explored in greater detail in § 3.3.2. No consistent trend was observed linking impedance performance at any frequency to *in vivo* signal acquisition for functional electrodes, a pattern that held across all seven CC MEAs that were implanted for acute recordings during this study. However, non-functional electrodes were able to be effectively identified and eliminated from data collection.

These findings prompted further analysis of the predictive value of impedance and led to the development of a dedicated recording system.

Given the ongoing debate regarding the role of impedance in predicting *in vivo* SNR [10, 11, 13–15, 23–27, 47]. The same CC MEAs used during bench-top characterisation were subsequently implanted<sup>29</sup> in Long Evans rats (*Rattus norvegicus*). Animals were anaesthetised with isoflurane, and all implantations described in this study were conducted acutely. This approach enabled direct comparison between bench-top characterisation and *in vivo* performance.

Here, no clear trend was observed between impedance and *in vivo* SNR, which is reported as a unitless ratio, as shown in Figure 12. That is, electrodes with lower impedance did not demonstrate preferential signal acquisition or higher SNR. This finding was consistent across all implanted MEAs. Spearman’s rank correlation indicated that impedance at  $f = 1\text{ kHz}$  showed no significant monotonic<sup>30</sup> relationship with *in vivo* SNR ( $\rho = -0.072$ ,  $p = 0.770$ ). Furthermore, Levene’s test<sup>31</sup> indicated no significant difference in signal variance *in vivo* across impedance values ( $W = 1.166$ ,  $p = 0.337$ ). No evidence was found to support the optimisation of impedance as a means to improve *in vivo* SNR in functional electrodes. This is in direct disagreement with the studies that reported a link between SNR and impedance [11, 15, 24–27, 47], but agrees with those disputing the relationship [10, 13, 14, 23]. Impedance magnitude at 15 Hz showed no relationship with *in vivo* SNR, despite suggestions to the contrary by Harris *et al.* [25] (Figure A1, Appendix A).

Therefore, these data suggest that once impedance falls below a certain threshold, further reduction has little to no effect on *in vivo* functional performance. In the context of developing MEAs, this is a notable finding for CC. While it is common practice to prioritise impedance minimisation during electrode fabrication and selection, Figure 12 demonstrates that this may not be necessary. Rather than targeting the lowest possible impedance, design efforts might be better focused on factors more directly linked to recording fidelity. This observation emphasises the need for a more holistic approach to considering shortcomings with poor performance from MEAs produced, outside of purely hardware considerations. Implying that biological and surgical procedures might be more important parameters to explore.

---

<sup>29</sup>For details on ethical approval, see [48], a manuscript currently in preparation.

<sup>30</sup>Spearman rank correlation quantifies the monotonicity of two variables.

<sup>31</sup>Levene’s test quantifies the variance between groups, i.e. do groups have same variability.

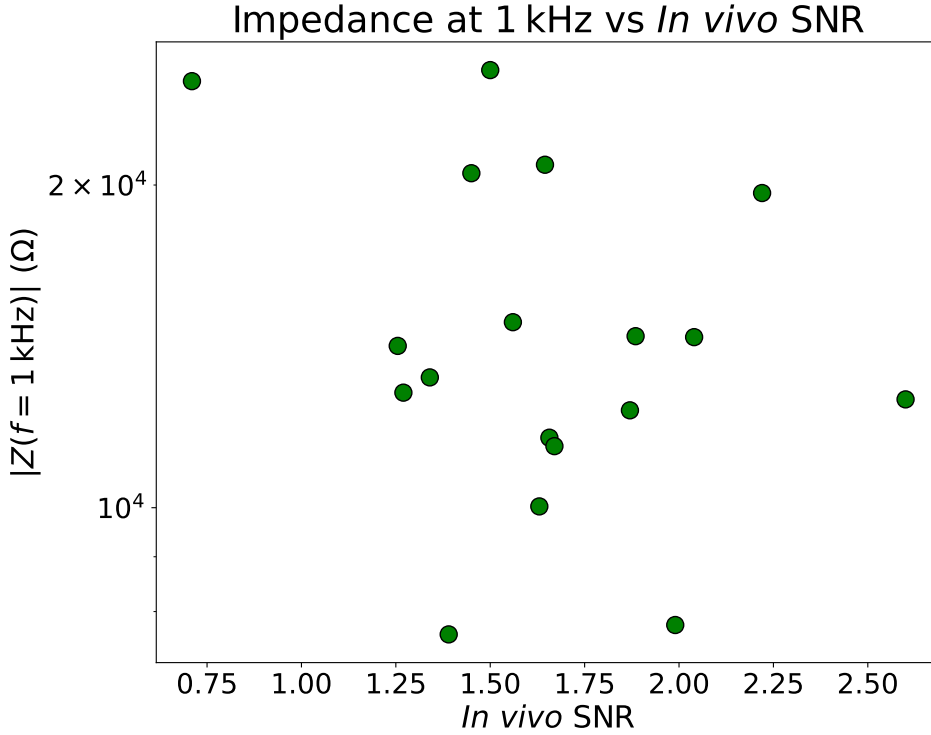


Figure 12. Plot of 1 kHz impedance magnitude versus *in vivo* SNR across CC MEAs. *In vivo* SNR was determined following spike sorting of neural recordings obtained from Long-Evans rats. No clear trend between impedance and *in vivo* SNR was observed. A similar lack of relationship at 15 Hz was observed (Figure A1, Appendix A).

## 3.2 Recording System

### 3.2.1 Oscilloscope

This study expands upon EIS characterisation by using the recording system to assess how individual MEA channels respond to external stimulation. The first aim was to identify channels that did not yield reproducible responses above baseline noise levels. Following this, trends were explored between bench-top recordings and *in vivo* measurements. The goal was to determine whether bench-top SNR characteristics could predict *in vivo* recording fidelity and identify optimal electrode parameters for *in vivo* acquisition [24, 27, 39].

Lewis *et al.* [24] previously used parallel plate electrodes to generate signals of various frequencies, which were recorded by a MEA at the centre of a 0.15 M saline bath. In contrast, other lab-built recording systems often use *in vitro* cell cultures [49–52]; however, these are typically employed to study cellular behaviour rather than to characterise MEAs. Chung *et al.* [27] used bench-top noise levels to determine electrode performance and this correlated with recording fidelity *in vivo*.

For a typical channel, the response to a biphasic stimulus is shown in Figure 13. The response obtained by a functional and non-functional channel is markedly distinct<sup>32</sup>, with the non-functional channel recording a small perturbation above the noise floor. As with EIS, non-functional channels failed to record spikes *in vivo*. In contrast, all functional channels consistently produce large responses to external stimulation.

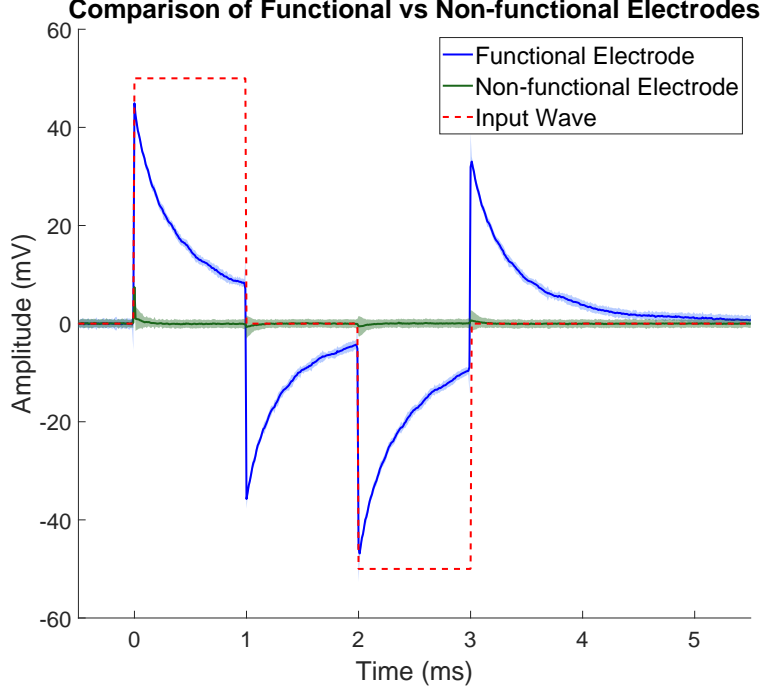


Figure 13. Comparison of typical averaged waveforms (from 900 events) recorded from a functional (blue) and a non-functional (green) MEA channel in response to a biphasic stimulation pulse (red) with an amplitude of 50 mV and a pulse width of 1 ms. Shaded regions represent  $\pm 1\sigma$ , indicating waveform variability. The functional response is highly consistent and reproducible across all functional electrodes and MEAs. The non-functional response, which shows minimal deflection and increased variability, is consistent across all non-functional electrodes and MEAs. The minimal response to the stimulus in non-functional channels is attributed to potential cross-talk. A custom-made stimulating electrode was used for stimulation

There is variation in the SNR of functional channels. Whereas, non-functional channels report an SNR of 0, as they record no clear signal distinguishable from noise (Eq. 5). The SNR for different channels on a typical MEA is shown in Figure 14.

This screening reliably separates functional and non-functional channels, performing comparably to EIS. That is, channels without bars in Figure 14 failed to pick-up *in vivo* spikes in all instances. This raises the question of whether the SNR of functional channels trend with *in vivo* data (Fig. 15).

---

<sup>32</sup>The shape of the waveform and stimulating electrode dependence is described in § 3.2.3.

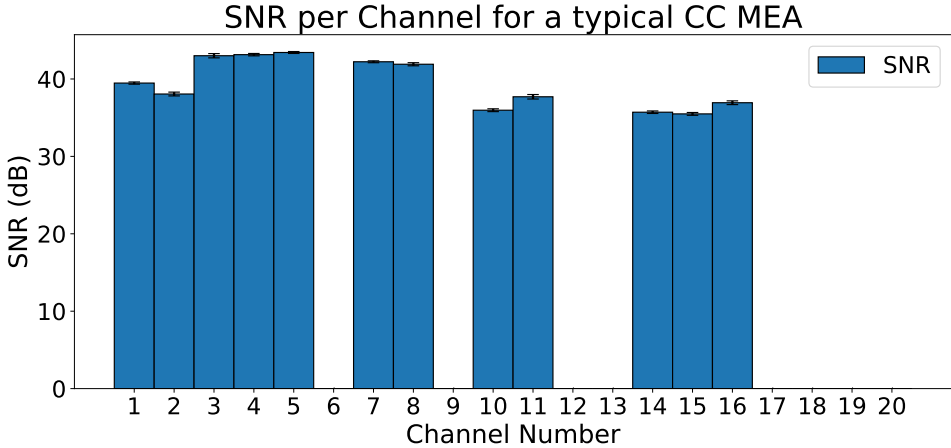


Figure 14. Plot of SNR against channel number of a typical CC MEA. SNR values of functional channels vary from 36 dB to 43 dB. Non-functional channels (6,9,12,13,17–20) show an SNR = 0. Error bars are based on propagated error (Eq. 5) and the  $\sigma$  of  $\langle V_{PP} \rangle$ .

In Figure 15, functional channels are plotted for bench-top SNR, obtained using the oscilloscope, against *in vivo* SNR. Here, no clear trend was observed between bench-top SNR and *in vivo* SNR. This finding was consistent across all implanted MEAs. Spearman’s rank correlation indicated that the bench-top SNR showed no significant monotonic relationship with *in vivo* SNR ( $\rho = -0.086$ ,  $p = 0.761$ ). Furthermore, Levene’s test indicated no significant difference in the spread of *in vivo* signal detection across bench-top SNR values ( $W = 1.084$ ,  $p = 0.369$ ). That is, there is no preferred bench-top SNR values, within the range of 37 dB to 42 dB for the optimisation of *in vivo* SNR of functional channels.

This partially disagrees with Lewis *et al.* [24], where performance differences were more pronounced due to variation in electrode coatings. In the present study, MEAs are produced using the same coating (PEDOT), so intra-MEA comparisons are expected to deviate less significantly. Hence, it is somewhat unsurprising that the trend between bench-top SNR and *in vivo* SNR is absent. However, additional testing on non-PEDOT coated electrodes revealed that they failed to detect signals under the same stimulation conditions. To obtain a measurable response, the stimulus amplitude had to be increased by a multiple. This highlights the sensitivity of the recording system to differences in surface coating, even though such electrodes were not implanted and therefore cannot be directly compared with *in vivo* data.

To assess whether impedance and bench-top SNR merely captured overlapping information, their relationship was evaluated. No significant correlation was observed between the two metrics, and neither showed a meaningful relationship with *in vivo* SNR (Appendix, Fig. A2)

The results obtained using the recording system provide independent evidence suggesting that bench-top metrics do not reliably predict recording fidelity. While this data is based on signal detection from a known stimulus, the poor relationship with *in vivo* performance reinforces the idea that hardware measures, whether electrical or otherwise, are insufficient

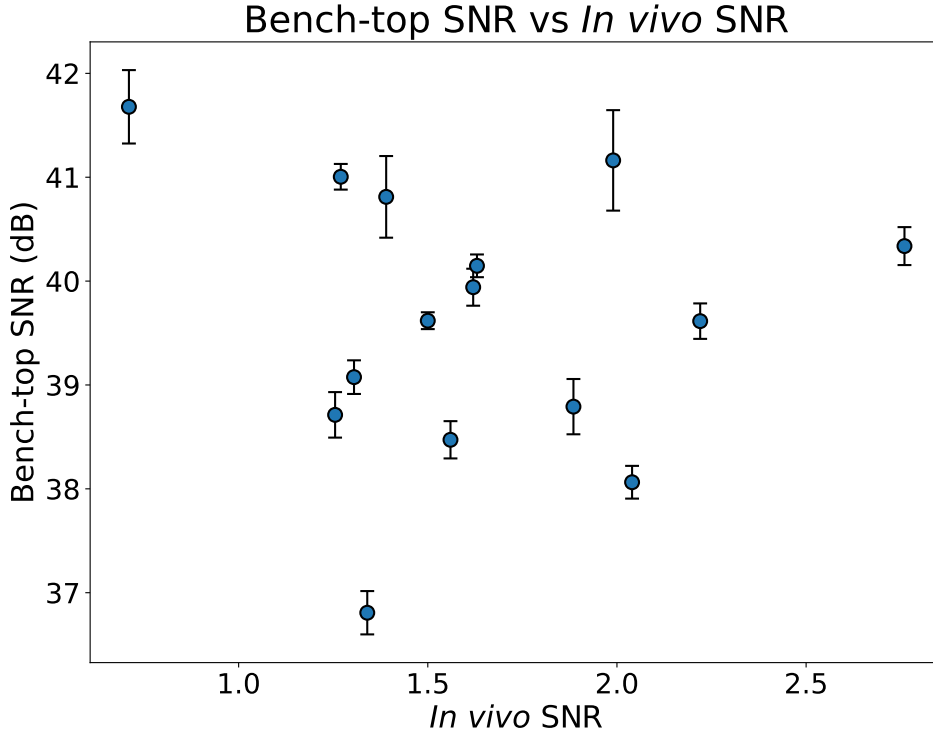


Figure 15. Plot of bench-top SNR versus *in vivo* SNR across 4 separate CC MEAs. *In vivo* SNR was determined following spike sorting of neural recordings obtained from Long-Evans rats. No clear trend between bench-top SNR and *in vivo* SNR was observed.

for optimising *in vivo* performance beyond basic screening. Furthermore, as with screening from EIS, only a finite fraction of functional electrodes successfully recorded signals after implantation. This strengthens the case that biological variability [28, 53, 54], surgical factors [55–57], and electrode positioning relative to a neuron likely play a more dominant role in determining recording quality.

A comparable analysis was also performed using the RGS, which showed the same overall trends observed here with the oscilloscope. To avoid redundancy, data is not shown here, however this finding highlights consistency across recording systems.

### 3.2.2 Ripple Grapevine System and Spatial Selectivity

In addition to the oscilloscope, the RGS was also used for bench-top recording. The RGS, designed for *in vivo* recordings, includes onboard analogue filtering and amplification that enables reliable detection of neural-scale signals during bench-top testing. It can measure voltage transients around  $\sim 100 \mu\text{V}$  [43], comparable to neural APs [19, 25, 52].

The biphasic stimulus waveform and stimulating electrode used initially mirrored those in the oscilloscope experiments. The input amplitude was reduced to 1 mV, the DAQ's lowest

reliable output, to test whether signal amplitude influenced the MEAs ability to distinguish signal from noise at the neural-scale. Under these conditions, functional channels recorded signals with peak amplitudes up to  $\sim 800 \mu\text{V}$ . Typically, non-functional channels exhibited only noise, although the noise level was often higher than that of functional channels ( $\sigma_{\text{non-func}} \approx 44 \mu\text{V}$ ,  $\sigma_{\text{func}} \approx 15 \mu\text{V}$ ). Representative traces for functional and non-functional channels are shown in Figure 16, confirming that the RGS is equally effective in identifying electrode functionality.

Despite the comparable screening outcomes, the RGS offers several practical advantages. Unlike the oscilloscope, which records only one MEA channel at a time, the RGS supports simultaneous recording across up to 32, accelerating data acquisition. Furthermore, by recording all channels simultaneously, it enables the analysis of spatial selectivity and cross-talk across the array. These analyses help identify shorted or non-functional channels.

However, the increased performance is accompanied by a substantial cost: the RGS system costs approximately 50,000 AUD, compared to under 1,000 AUD for the oscilloscope. Thus, while both systems can assess electrode functionality, the RGS is over-specified for routine screening. Using the oscilloscope presents itself as a more practical and cost-effective solution.

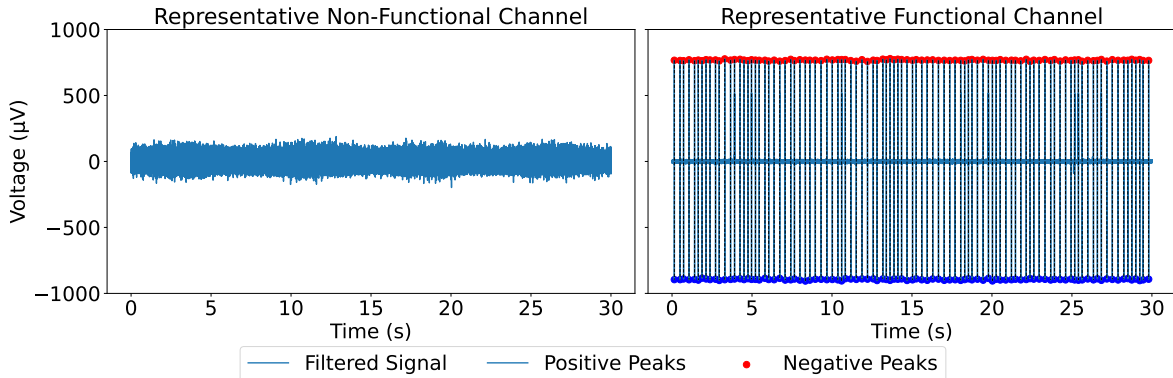


Figure 16. Filtered voltage traces (bandpass: 50 Hz to 2000 Hz) of  $V(t)$  recorded from representative electrodes during stimulation with a  $2 \text{ mV}_{\text{pp}}$  biphasic waveform. Data were acquired using the RGS. Left: Trace from a non-functional electrode, where no signals are detected and only background noise is visible. Right: Trace from a functional electrode, clearly displaying the biphasic pulses with consistent signal detection. Dashed black lines indicate the vertical extent of individual waveforms. Red and blue dots mark positive and negative peaks, respectively, used to compute  $V_{\text{PP}}$  and estimate the SNR.

When using the standard stimulating electrode, all functional channels measured roughly the same input signal without spatial selectivity, limiting the ability to explore cross-talk and the functional resolution of the MEA.

Therefore, to explore spatial selectivity, a patch-clamp electrode was used for its reduced size and higher impedance compared to the stimulating electrode detailed previously. A similar concept was demonstrated by Viswam *et al.* [39], who used high-density planar arrays and high-impedance patch-clamp stimulating electrodes to observe spatial selectivity.

A patch-clamp electrode acts as a quasi-point source, enabling precise spatial probing of individual fibres on a CC MEA. As it was moved away from a fibre, the signal recorded rapidly diminished, indicating highly localised signal detection.

As shown in Figure 17, a clear power-law decay ( $\propto r^{-2}$ ) is observed with respect to distance. Signals were recorded up to 200  $\mu\text{m}$  from the defined origin, but distinguishable signals were only observed within 140  $\mu\text{m}$ . The SNR plateaued at approximately 12.5 dB before dropping to 0, corresponding to the point at which peaks were no longer detectable relative to noise. This is valuable for two key reasons. First, it is physically consistent with the commonly assumed qualitative distance of approximately 100  $\mu\text{m}$  required to record a signal from a neuron using a CC MEA. This distance is based on experimental experience in the group, although it is not formally established in the published literature. Secondly, because this decay length is smaller than the pitch spacing of the current arrays (500  $\mu\text{m}$ ), it provides a means to study cross-talk between channels on an MEA. The signal detected by adjacent channels should be fully attenuated in the absence of cross-talk.

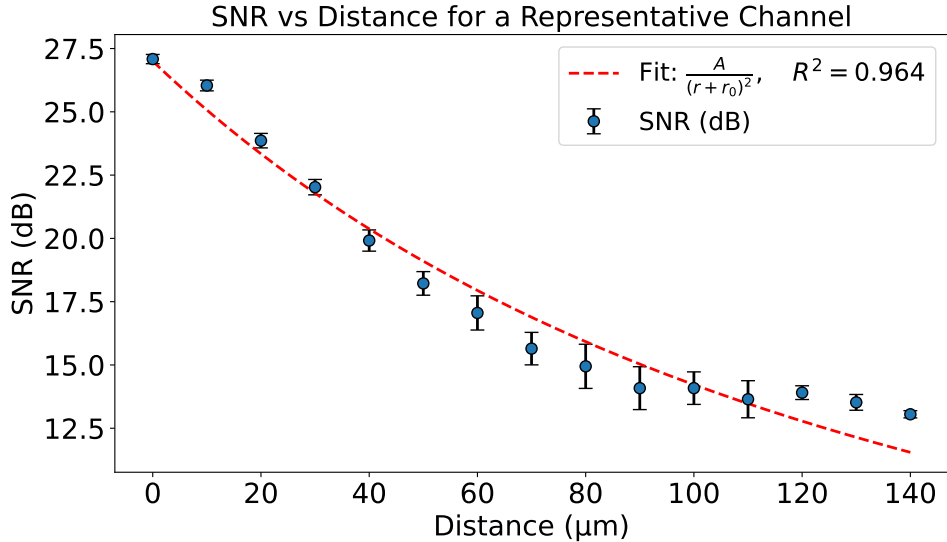


Figure 17. Bench-top SNR as a function of distance ( $\mu\text{m}$ ) from the patch-clamp pipette for a representative electrode. Signals were recorded up to 200  $\mu\text{m}$  away, but reliable spike detection was only observed within the first 140  $\mu\text{m}$ . The fitted inverse-square model of the form  $\frac{A}{(r+r_0)^2}$  is shown in red and demonstrates strong agreement with the data ( $R^2 = 0.964$ ).

McNamara *et al.* [58] proposed a protocol for quantifying cross-talk in neurostimulation electrodes, in which current pulses were applied directly through one channel and the resulting response was measured on adjacent channels. Their results demonstrated the utility of such procedures for assessing both recording and stimulation cross-talk in MEAs. In the aforementioned study, two channels were intentionally bridged, and the resulting cross-talk was successfully detected using the proposed method.

In this present study, cross-talk was assessed by sequentially stimulating each channel using a patch-clamp electrode above each carbon fibre of a CC MEA. In contrast to previous

work [58], direct stimulation to the channels was intentionally avoided, due to the risk of potentially damaging the PEDOT coating. Since the same MEA is later implanted *in vivo*, it was essential that all bench-top testing remain entirely non-destructive. This approach served both to verify individual channel functionality and to reveal any unintended signals on adjacent electrodes.

To demonstrate the relevance of the selectivity of the patch-clamp electrode set-up, a representative bar plot is shown in Figure 18, illustrating the result of stimulation above channel 2. Similar results were obtained across active electrodes when the stimulating electrode was placed above them (Fig. A3, Appendix A). The mean peak-to-peak voltage,  $\langle V_{PP} \rangle$ , is plotted for each channel, showing the largest response on the intentionally stimulated channel. Figure 18 shows that the intentionally stimulated Channel 2 recorded a  $\langle V_{PP} \rangle$  of approximately 1250  $\mu$ V, while all other channels recorded significantly smaller signals. This indicates an absence of significant cross-talk between Channel 2 and the other channels on the MEA. Similar responses were observed across all stimulated channels, suggesting negligible cross-talk on this device. Cross-talk could affect the reliability of *in vivo* recordings, as the same neuron may be falsely detected across multiple channels. Therefore, this pre-implantation screening provides valuable insight during the spike-sorting process, allowing for the mitigation of errors.

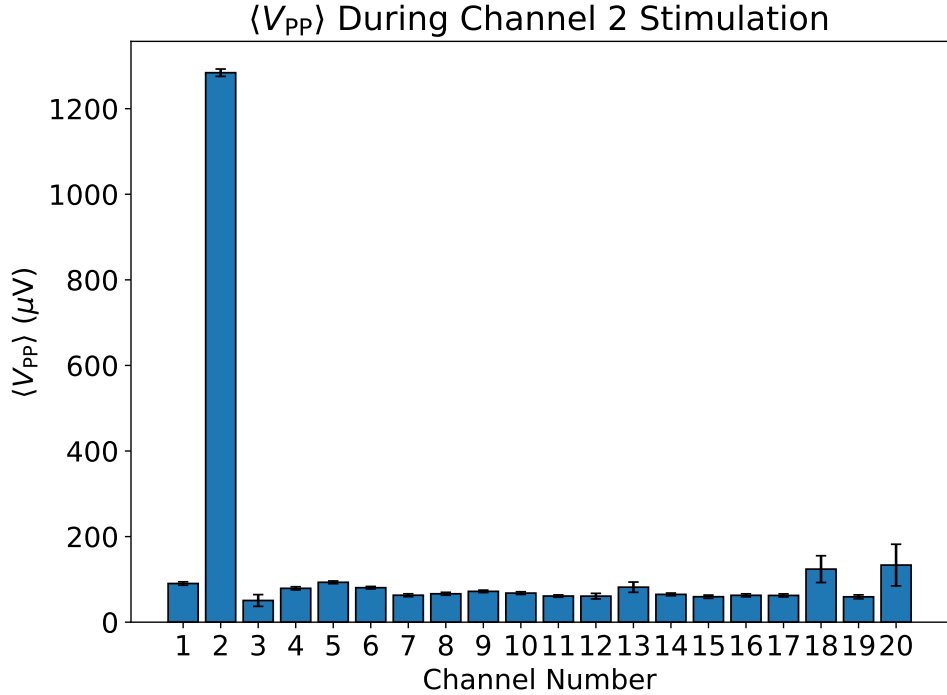


Figure 18. Bar plots showing the  $\langle V_{PP} \rangle$  of all 20 channels on a CC MEA. The patch-clamp electrode was positioned approximately 5  $\mu$ m from Channel 2. No observable cross-talk was detected between Channel 2 and adjacent channels. This plot is representative of the behaviour observed across all channels (Figure A3, Appendix A).

This method was evaluated using a single CC MEA with 20 connected fibres, due to limited

device availability. As such, the generalisability of the results is limited, and the conclusions should be considered tentative. Furthermore, there is a limitation with respect to the positioning of the patch-clamp electrode relative to the carbon-fibre being probed on the MEA. Despite care being taken to align the electrode above each channel, the depth of the optical microscope made it challenging to know the precise displacement from the tip of the carbon fibre. Variability in proximity would affect the local field strength measured from the patch-clamp (Fig. 17), introducing some stimulation-dependent variation to the recorded signal amplitude. Nonetheless, across all measured channels, it was observed that the response from the intentionally stimulated channel consistently exceeded that of surrounding channels. Correlation-based methods were not used, as they did not yield additional information [59].

### 3.2.3 Dependence of stimulating electrode

Throughout the experiments, the recorded signals were strongly influenced by the properties of the stimulating electrode. The choice of stimulating electrode significantly affected the shape of the recorded waveform, likely due to changes in capacitance. Capacitance scales linearly with surface area<sup>33</sup>. As a result, larger electrodes exhibit greater double-layer capacitance, as described by

$$C_{dl} = c_{dl} \cdot A \quad (9)$$

where  $C_{dl}$  is the double-layer capacitance,  $c_{dl}$  is the specific (area-independent) double-layer capacitance, and  $A$  is the surface area of the electrode. The value of  $c_{dl}$  is a property of the electrode-electrolyte interface and varies with the material [36].

Stimulating electrodes with small geometric surface areas, and therefore lower  $C_{dl}$ , were associated with distinct recording waveforms, shown in Figure 19a. This decay consistently varied with the stimulating electrode, while the recording MEA remained unchanged, suggesting it reflects properties of the stimulator rather than the MEA itself. A shorter decay time was observed when using a laser-deinsulated carbon fibre electrode (6  $\mu\text{m}$  diameter, 50  $\mu\text{m}$  exposed length; Fig. 19a). In contrast, a larger stimulating electrode, such as a 500  $\mu\text{m}$  wire, produced a signal that more closely resembled the applied square wave. A slower decay was still visible (Fig. 19b). According to Equation 9, increasing the electrode surface area increases the double-layer capacitance. While material differences affect this relationship, the observed trends match the expected physical behaviour.

As shown in Panels (c) and (d) of Figure 19, exponential fits were used to extract a time constant,  $\tau$ , for each waveform. Capacitance values for the stimulating electrodes were independently determined from EIS measurements (via Equation 3, using a least-squares simplex fit). In general, larger  $\tau$  values were observed for electrodes with higher capacitance, consistent with expectation.

From this assessment, it is evident that the polarisation and capacitive behaviour of the stimulating electrode must be accounted for when using a bench-top recording system to

---

<sup>33</sup>Surface coatings introduce porosity, meaning factors beyond the geometric surface area influence capacitance [24].

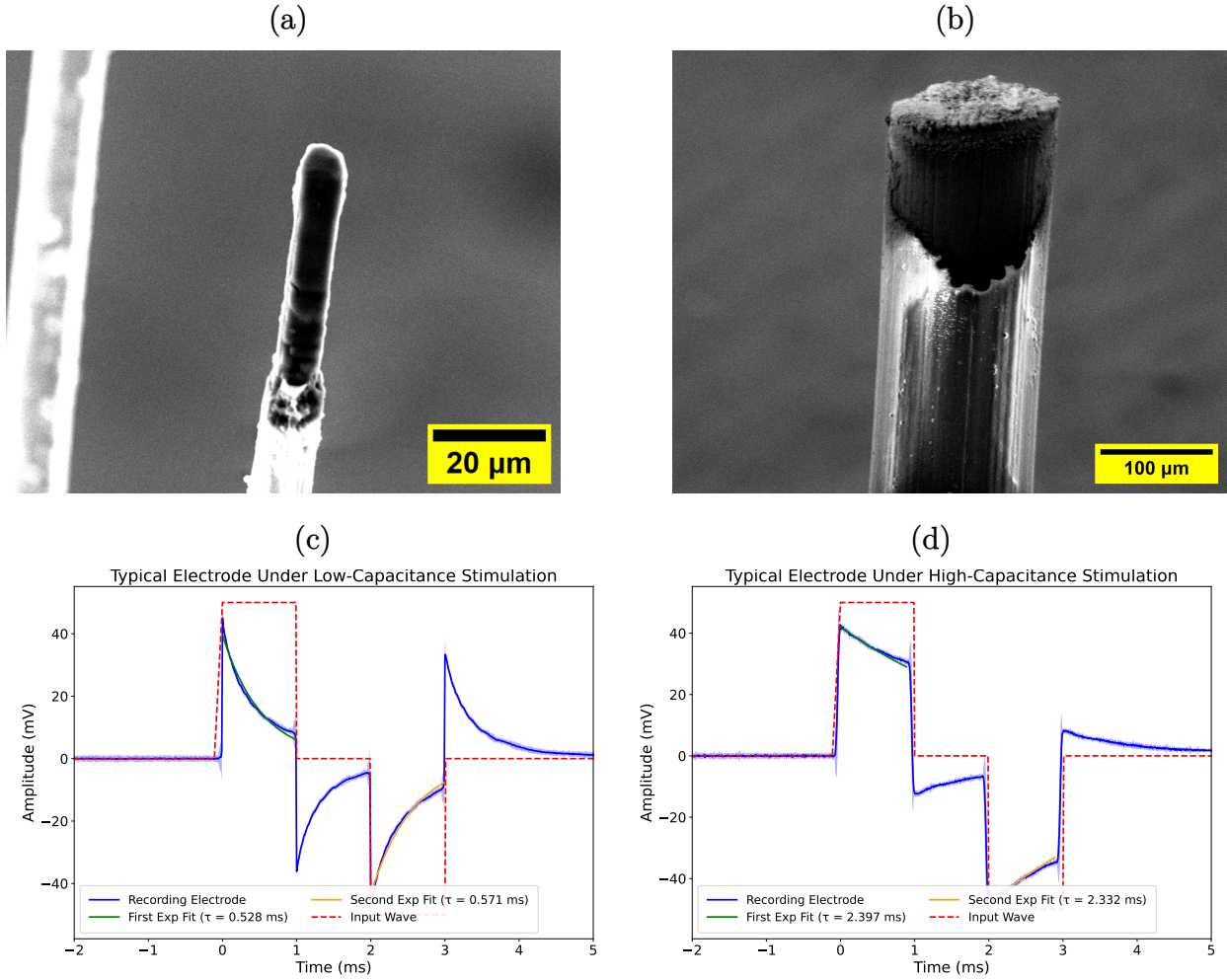


Figure 19. (a) SEM image of a single carbon fibre electrode used for stimulation testing. ImageJ was used to determine the fibre's exposed length and diameter using the known scale bar. As PEDOT is conductive and Parylene-C is insulating, the PEDOT-coated region appears darker, while the Parylene-C-insulated region appears lighter.

Capacitance:  $1.67(96) \times 10^{-7}$  F; Scale bar: 50 μm. (b) SEM image of a typical tungsten wire used for testing MEAs. The de-insulated region near the end of the fibre appears darker, while the insulated bulk region appears lighter. The tip of the wire is lighter and less conductive than the exposed bulk, attributed to the formation of  $\text{WO}_3$  during the laser de-insulation process.  $\text{WO}_3$  is highly resistive at room temperature [60].

Capacitance:  $1.160(35) \times 10^{-5}$  F; Scale bar: 200 μm (c) Average waveform recorded by an MEA in response to stimulation from a low-capacitance source (a) with  $\langle\tau\rangle = 0.630(30)$  ms.

(d) Average waveform recorded in response to a high-capacitance source (b), yielding  $\langle\tau\rangle = 2.36(5)$  ms. In both (c) and (d), the dashed red line shows the input waveform, while the blue trace is the recording from the MEA, with the shaded region indicating  $\pm\sigma$ . Exponential fits shown in green and orange are used to calculate  $\tau$ .

assess the recording performance of MEAs. The observed exponential behaviour (Panels (c) and (d), Fig. 19) reflects the properties of the stimulating electrode and is not intrinsic to the recording MEA. However, intra-array SNR trends remained consistent when only the initial response, at the onset of stimulation, was analysed. This holds true if sufficient time is also allowed between stimulation peaks for the system to reach equilibrium,  $\langle V \rangle \rightarrow 0$ . Together, these observations demonstrate that in any system designed for the characterisation of MEAs, the stimulating electrode must be thoroughly characterised and well understood. Ideally, the effects of the stimulating electrode should be easily isolated in order to reliably interpret the true performance of the recording MEA. To ensure consistency, the same stimulating electrode and the same pulse parameters were used across all reported metrics when reporting SNR.

### 3.3 Understanding the limits of bench-top testing

Having presented the key bench-top characterisation results, this sub-section critically evaluates the limitations of the recording system and disconnect between bench-top metrics and *in vivo* performance, drawing on existing literature [23, 55, 56, 61] and a contextual analysis of existing *in vivo* data.

#### 3.3.1 Limitations to the experimental methodology

Several limitations affecting the predictive capability of bench-top characterisation methods for optimising *in vivo* performance were identified, warranting further investigation.

The central challenge of this study was not in developing a more sensitive recording system, but was addressing the fundamental limitations of bench-top techniques in predicting *in vivo* performance. Consistent with previous reports [10, 23], the present findings reaffirm the limited predictive power of bench-top characterisation methods. However, the system developed here demonstrates clear utility as a cost-effective tool for reliably screening functional electrodes. Given the time and financial costs of fabricating MEAs and conducting *in vivo* experiments, it is important to increase the likelihood of experimental success. A system like this can help by ensuring that only MEAs with a sufficient number of functional channels are implanted.

However, no clear relationship was observed between bench-top SNR measurements and *in vivo* recording performance beyond screening for functional channels. As such, aside from its cost advantage compared to EIS with a potentiostat, the broader utility of this recording system remains limited without further validation.

Furthermore, SNR values reported here are consistently higher than those observed *in vivo*. This is largely due to the magnitude of the signal input, which directly inflates the bench-top SNR obtained. Pulse parameters were kept consistent throughout reporting to minimise variability. In addition, as noted by Cogan [61], tissue resistance is much greater than the

resistance found in an electrode-electrolyte setup. For the same input current, the voltage transient measured in saline is three times larger in the electrode-electrolyte setup than in *in vivo* measurements [61]. Therefore, even with the same input signal ( $V_{\text{in}} \approx |\text{AP}|$ ), SNR will be higher in the bench-top setup.

Finally, optimising electrodes for recording performance and insertion efficacy presents distinct yet related challenges. For example, increasing the size of an electrode may significantly improve bench-top recording performance, but it can also increase insertion force, the likelihood of buckling, and the severity of the potential Foreign Body Response (FBR) [16]. These are challenges that carbon fibre-based MEAs are specifically designed to address [11, 17]. These trade-offs cannot be easily assessed using the current recording system or EIS and therefore must be considered through tests independent of those explored in the present study.

Across both impedance-based and bench-top SNR screening methods, a key observation emerged. Not all electrodes classified as functional ultimately recorded spikes *in vivo*. Functional classification was defined by impedance below a specified threshold or by recording a measurable response to electrical stimulation in 0.15 M saline. Channels that did not meet these criteria consistently failed to record neural activity *in vivo*. Despite meeting these criteria, a significant number of functional electrodes per MEA consistently fail to record neural activity. Although this phenomenon has been recognised [11, 17, 18, 23], it is often not explicitly investigated. For example, Neto *et al.* [23] report recordings from 11 implantations using 32-channel MEAs. However, only around 100 neurons were recorded in total. This implies that a substantial fraction of functional electrodes failed to yield successful recordings, as  $11 \times 32$  should have yielded 352 neurons if all the electrodes were picking up signals. That is only 28.4% of the total electrodes picking up signals. Likewise, Massey *et al.* [17] found that only 63% of the total channels recorded signals, although achieving this required three insertions. Furthermore, Neuralink has found that an average of only 47% of electrodes work once implanted in human patients [62]. Consequently, the typical fraction of functional electrodes expected to record successfully remains under-reported, especially in the context of MEAs that have been screened and then implanted *in vivo*.

This was bolstered by the qualitative observation, by CC, that some channels only recorded neural spikes on the second or third insertion. This suggests that biological variability, and possibly surgical considerations, may dominate hardware concerns [53, 55, 56, 63]. This highlights a potential, critically important, limitation in the predictive power of current screening techniques. To further investigate this phenomenon, the following section considers the performance of commercially manufactured MEAs (Neuronexus) across three animal models. This broader analysis aims to assess whether this disconnect persists across species, where all electrodes on the MEA are reasonably expected to be functional. This allows for the exploration of possible biological factors contributing to this outcome.

### 3.3.2 Re-analysis of *in vivo* data

Existing *in vivo* datasets<sup>34</sup> collected by Jung *et al.* [29], Jung [48] and Almasi *et al.* [64, 65] were re-analysed to quantify the variability in the fraction of signals recorded for functional MEAs across species. Although it has been qualitatively observed by CC that the number of channels recording neural signals varies between animal models this variability has not been quantitatively assessed in the context of MEA performance. In these datasets, commercial MEAs (Neuronexus<sup>35</sup>; A1×32 and A4×8) were used, standardising the recording electrode and ensuring consistency in recording hardware. The use of commercial MEAs supports the assumption of a high degree of functionality across channels. The fraction of electrodes that successfully recorded neural signals was evaluated across three animal models: wallabies [28, 29], rats [48], and cats [64, 65]. The results reveal substantial variability both within and between species.

Over 150 hours of *in vivo* recordings were analysed. Data from seven wallabies, each with at least three insertion depths, and seven rats, with one to three insertions each, were included, along with six cats, each with multiple insertions. The detection rate of channels recording signals as a function of depth was calculated for the three animal models and is shown in Figure 20. It is expected that neuron density varies with insertion depth and influences the expected number of signals obtained [63].

The analysis showed that the choice of animal model and the depth of electrode insertion are major factors in determining whether an individual electrode successfully records *in vivo*. However, it remains difficult to quantify these factors with bench-top tests, as variability persists *in vivo*, limiting what can be achieved through bench-top testing. Figure 20 shows average yields of 66(4) %, 34(4) %, and 65(4) % for wallabies, rats, and cats, respectively. These values are consistent with those calculated from Massey *et al.* [17] and Neto *et al.* [23]. These results show that, when combined with bench-top testing, *in vivo* data can be used to estimate the number of channels likely to detect spikes on a MEA. Unpaired *t*-tests were performed and reveal highly significant depth-dependent variation in the fraction of electrodes recording signals ( $p < 0.0001$ ). Rat data showed a sharp increase in detection rate up to 2100  $\mu\text{m}$ , where it plateaued. Wallaby data showed a general increase in detection rate with depth, though this was inconsistent, and cat data appeared to peak between 2000  $\mu\text{m}$  to 3000  $\mu\text{m}$ . Negative depths likely arose from brain swelling or human error in defining the zero point at the brain surface.

Together with the present analysis, two independent studies by Fiath *et al.* [55, 56] provide further evidence that biological and surgical factors substantially influence recording yield. The former found that detection rates differ between edge and centre channels within a single-shank array, while the latter showed that insertion speed significantly impacts *in vivo* recordings. These findings suggest that biological and surgical factors may have a greater influence on electrode performance than can be predicted by bench-top optimisation of impedance or SNR metrics.

---

<sup>34</sup>For full details on the *in vivo* procedure and associated ethical approvals, see [28, 29, 48, 64, 65].

<sup>35</sup><https://www.neuronexus.com/>

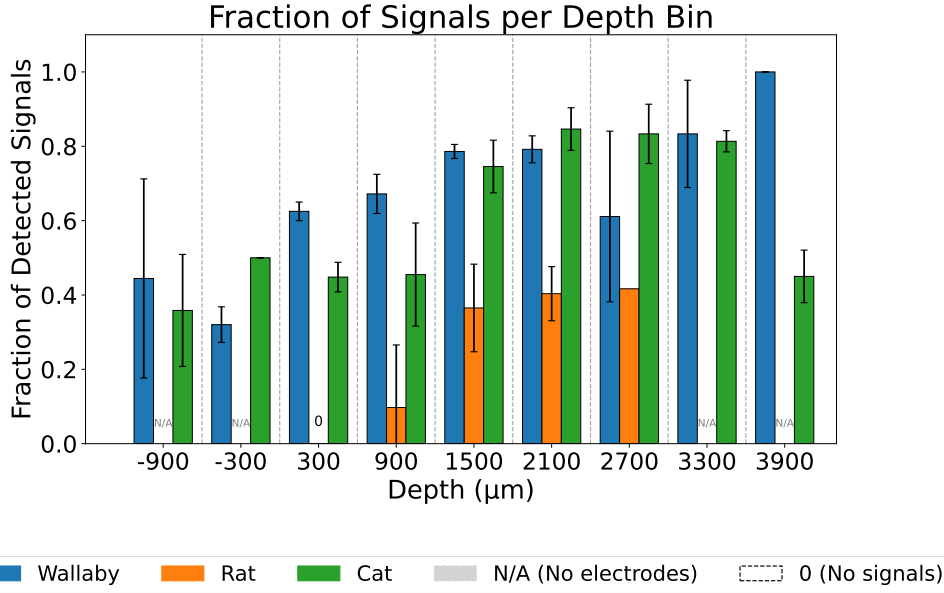


Figure 20. Bar plots showing the depth of insertion on the *x*-axis and the fraction of channels that recorded a signal on the *y*-axis, for rat, wallaby, and cat datasets. Data were binned into 600  $\mu\text{m}$  intervals, represented by the vertical dashed gray lines. Error bars represent the standard deviation within each bin, calculated from 200  $\mu\text{m}$  sub-bins. Data were obtained using assorted 32-channel Neuronexus probes, including both single-shank and four-shank configurations. Rat data exhibit a general increase in signal yield with depth, which plateaus beyond 2100  $\mu\text{m}$ , with an average signal fraction of 34(4)% across all depths. Wallaby data also increase with depth, though negative depths suggest brain movement post-insertion, with an average signal fraction of 66(4)%. Cat data show a peak in signal fraction between 2000  $\mu\text{m}$  to 3000  $\mu\text{m}$ , followed by a decline at greater depths and an average signal fraction of 65(4)%, with similar movement-related negative depths. The three species demonstrate distinct depth-dependent recording profiles.

To explore the observed differences in *in vivo* detection rates between species, a probabilistic model was developed as a conceptual tool to examine how species-dependent factors, such as neuron density and anaesthetic, might affect the probability of detecting neural signals. The model integrates geometric constraints, based on experimental work, with biological parameters to provide a framework for interpreting observed yield differences between animal models. In doing so, it supports a wider discussion around the limitations that influence bench-top testing for predicting recording fidelity *in vivo*.

### 3.3.3 Towards a Computational model based on *in vivo* data

The rat and cat data<sup>36</sup> were used to develop a simple probabilistic model that estimates the probability of signal detection as a function of neuron density. This model is motivated by

<sup>36</sup>The wallaby data were not used in the development of the model, as no reliable source for the average neuron density exists; see Table 1.

the large variation in neuron densities between species (Tab. 1), which likely contributes to varying detection rates across animal models [53]. This provides a framework for reasoning about recording yields in new species, including humans. While the neuron density in humans is known, the recording yield, given the surgical procedures used for CC electrodes, is not.

Table 1. Mean and standard error of V1 neuron counts and surface densities, with mean cortical area, for selected species. Table modified from Weigand *et al.* [53].

Species	$n$ (neurons)	$A$ ( $\text{mm}^2$ )	$n/A$ ( $\text{mm}^{-2}$ )	Refs.
<i>Rattus norvegicus</i>	$720,000 \pm 100,000$	8.5	$85,000 \pm 10,000$	[66–71]
<i>Felis catus</i>	$31,000,000 \pm 4,000,000$	345	$88,000 \pm 10,000$	[66, 67, 72]
<i>Homo sapiens</i>	$575,000,000 \pm 200,000,000$	3,830	$150,000 \pm 50,000$	[73, 74]
<i>Ovis aries</i> <sup>a</sup>	18,000,000	1000	18,000	[53]
<i>Macropus eugenii</i> <sup>b</sup>	—	—	—	—

<sup>a</sup> *Ovis aries* (Sheep) is an estimate provided by Weigand *et al.* [53] without specified uncertainty.

<sup>b</sup> To the best of our knowledge, no direct measurements currently exist for *Macropus eugenii* (Tamar Wallaby) neuron density.

In this model, the electrode is represented as a cylinder with a hemispherical tip, as demonstrated in Figure 21. This approximates an electrode inserted into isotropic, homogeneous brain tissue with a known neuron density. Neurons are assumed to be equally spaced. The maximum distance of a measurable neuron from a recording electrode,  $R_d$ , is set to 140  $\mu\text{m}$ , based on the value determined from the bench-top spatial selectivity testing (Fig. 17).

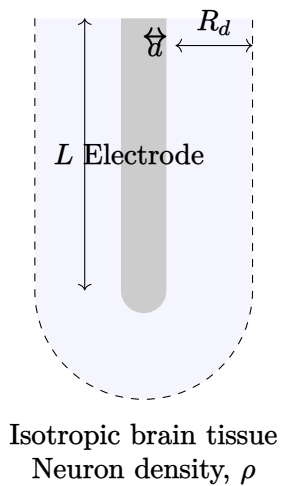


Figure 21. Schematic of a single electrode inserted into isotropic brain tissue, illustrating the detection radius  $R_d$ , electrode length  $L$ , and radius  $a$ . The detection radius  $R_d$  defines the cylindrical region surrounding the electrode within which neural signals may be detected. This model is used to estimate the probability of detecting neural signals as a function of neuron density  $\rho$ .

The number of neurons in an electrode's detectable region is defined as

$$\lambda = \rho \cdot V_{\text{detect}}, \quad (10)$$

where  $\rho$  is the neuron density,  $V_{\text{detect}}$  is the detectable region around the electrode,  $\lambda$  is the number of neurons in this region,  $R_d$  is the detection radius and  $a$  is the physical radius of the electrode.

The approximate volume of the detectable region is

$$V_{\text{detect}} = \pi L (R_d^2 + aR_d), \quad (11)$$

and the number of neurons,  $\lambda$ , with

$$\lambda = \rho \cdot \pi L (R_d^2 + aR_d). \quad (12)$$

Based on *in vivo* measurements, the presence of a neuron within the detection radius does not guarantee it will be detected. If this were the case, one would expect near a 100 % yield in the fraction of detected signals based purely on the average neuron density. Poisson probabilities were used to determine the probability of an individual electrode detecting a signal, denoted as  $p_e$ . The parameter  $\alpha$  was introduced: it accounts for biological variability, where  $\alpha \in (0, 1]$ .

$\alpha$  is modelled using a power-law relationship of the form

$$\alpha = c \cdot \rho^b, \quad (13)$$

where  $c$  is a scaling constant, while  $b$  describes the dependence of  $\alpha$  on the neuron density  $\rho$ . This form was chosen based on its ability to fit the observed detection probabilities. These parameters were obtained by fitting the model to empirical data, minimising the squared error between predicted and empirical detection rates.

This leads to an expression for the probability of detection per electrode

$$p_e(\rho) = 1 - \exp (-c \cdot \rho^{b+1} \cdot \pi L (R_d^2 + aR_d)). \quad (14)$$

This can be re-expressed as

$$p_e(\rho) = 1 - \exp [-\alpha(\rho) \cdot \lambda(\rho)]. \quad (15)$$

However, the anaesthetic used between animal models varied and this is known to have a non-negligible effect on the neural activity recorded [57]. Of particular relevance here, the spiking rate<sup>37</sup> varies depending on the anaesthetic used. Isoflurane was used for rats, while halothane was used for cats and wallabies, this is typical for the anaesthesia of larger animal models [28, 29].

Villeneuve and Casanova [57] demonstrated that, even at the same Minimum Alveolar Concentration (MAC), defined as the “minimal anaesthetic concentration in the alveoli required

---

<sup>37</sup>Spiking rate refers to the number of APs generated by a neural population per unit time.

to keep an animal from responding by gross purposeful movement to a painful stimulus” [75], spontaneous<sup>38</sup> spiking rates differ. Using the same MAC ensures equivalent anaesthetic potency, so changes in spiking rate can be largely attributed to the interaction between the anaesthetic and the species.

Comparing isoflurane and halothane, there is a  $2.21 \pm 0.04$  fold reduction in spontaneous spike rate under isoflurane, based on values extracted from Villeneuve and Casanova [57] at equivalent MAC levels<sup>39</sup>.

To account for this, a correction factor  $\phi$  is introduced, which rescales neural responsiveness under isoflurane. In the model, this corresponds to a rescaling of the parameter  $\alpha(\rho)$  in Equation 15. The adjusted probability of detection thus becomes:

$$p_e(\rho) = 1 - \exp [-\phi \cdot \alpha(\rho) \cdot \lambda(\rho)], \quad (16)$$

where  $\phi_{\text{iso}} = 2.21 \pm 0.04$  and  $\phi_{\text{halo}} = 1$ .

The resulting detection probabilities for each species are shown in Figure 22, based on the known neuron densities (Tab. 1). The figure plots the probability of detecting at least eight distinct neurons, typically used as a minimum threshold in published studies [28]. The predicted probability based on the neuron density of sheep,  $p_e(\text{Sheep}) = 0.25 \pm 0.02$  is consistent with in-house recordings, where the yield from sheep was found to be extremely low. As a result, the group<sup>40</sup> largely discontinued use of sheep for this type of testing. Furthermore, the prediction based on the human neuron density,  $p_e(\text{Human}) = 0.81 \pm 0.05$ , is likely an overestimate, as Neuralink reported a 47% yield [62], though surgical parameters and anaesthetic conditions likely varied. Nonetheless, it suggests that, under current surgical procedures, signal yields in humans should exceed those in other species tested.

This model makes a number of assumptions and simplifications that should be noted. First, the brain tissue is assumed to be isotropic and homogeneous. However, in practice, tissue density exhibits spatial variation [63]. Second, neurons are treated as being equally spaced, although in reality, the presence of neuronal clusters and regions without neurons affects local neuron densities and, as a result, the model outcomes [28, 76]. Furthermore, the material properties and impedance of the electrode are not considered; instead, the optimisation is based on *in vivo* data. This data was acquired using commercial neuronexus MEAs, further deviations between these and the CC MEAs could plausibly exist - specifically with respect to the optimisation of  $\alpha$ . Each neuron and electrode is assumed to act entirely independently.

Moreover, since an empirical fit is employed, the model assumes that extrapolation between species is valid based solely on neuron density, without explicitly accounting for differences in cortical architecture [54]. However, Weigand *et al.* [53] argue that differences in neural

---

<sup>38</sup>Spontaneous means in the absence of deliberate external stimulation that assists in generation of APs [57]. Spontaneous APs are studied in [28, 29, 48, 64, 65]

<sup>39</sup>Spike rate values were estimated from Figure 7 of Villeneuve and Casanova [57] by visually extracting spontaneous activity at MAC values of 0.69, 1.0, and 1.38 for both anaesthetics. These were used to compute the mean fold reduction and standard error reported in the present study.

<sup>40</sup>These findings are based on internal observations from CC before the beginning of this project.

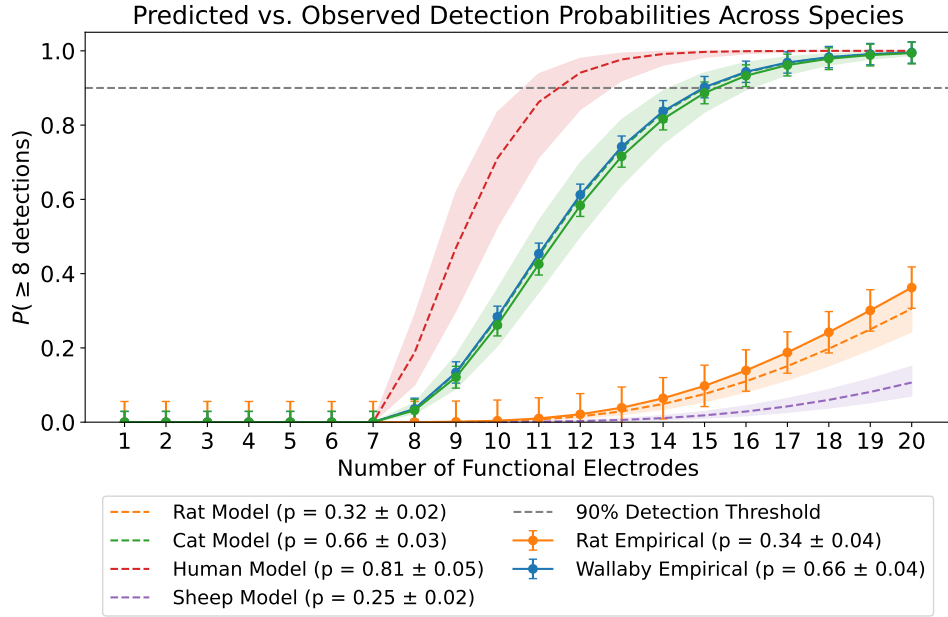


Figure 22. Comparison of empirical (solid lines with markers) and predicted (dashed lines) signal detection probabilities across various species. The neuron densities are those reported in Table 1. Error bars represent the standard error of the variation of detection probabilities across depth for each species. Rat data are shown without anaesthetic correction,  $\phi$ , to reflect measured detection rates. The model, however, applies the correction factor  $\phi$  to account for the suppressive effect of isoflurane relative to halothane when calculating the parameters. The dashed gray line indicates a 90 % confidence threshold. The model predicts a single-electrode detection probability of  $p_e(\text{Human}) = 0.81 \pm 0.05$  and  $p_e(\text{Sheep}) = 0.25 \pm 0.02$ . All electrodes are assumed to be functional, that is, they have passed screening tests.

structure between rodents, primates, and cats can be explained primarily by neuron density and total neuron number, without requiring species-specific differences in cortical architecture. Therefore, this assumption is considered reasonable. Nonetheless, as the fit is based on only two species with known neuron densities, the scope of the model remains limited, and its predictive power is constrained until further data become available.

Finally,  $p_e$  is assumed to increase monotonically with respect to  $\rho$ , although not necessarily in a linear way. Halothane is assumed in the model. For other anaesthetics, changes in spiking activity at a given MAC should be adjusted using the correction factor,  $\phi$ .

## 4 Conclusions

The findings presented here suggest that further optimisation of bench-top testing methods, such as EIS or the recording system, is unlikely to provide meaningful improvements in pre-

dicting *in vivo* recording performance. Across both commercial and CC MEAs, electrodes classified as functional showed a finite but variable chance of recording spikes, with outcomes more strongly influenced by biological and surgical factors than by intrinsic electrode properties.

Given this limitation, a more effective approach is to increase the number and density of recording channels. The spatial decay of detectable signals (140 µm) is considerably smaller than the current pitch spacing (550 µm), indicating that increasing channel density is feasible. Increasing the number of channels also improves the probability that a sufficient number will record *in vivo*.

Furthermore, optimising surgical factors such as anaesthetic choice, animal model selection, and insertion procedures is likely to have a more significant impact on detection rates. Together, these results support a shift in focus away from refining individual electrode metrics and toward improvements in overall MEA design and surgical methodology.

## References

- [1] R. P. Carlyon and T. Goehring, *Cochlear Implant Research and Development in the Twenty-first Century: A Critical Update*, Journal of the Association for Research in Otolaryngology **22**, 481 (2021), type: Journal Article.
- [2] I. Boisvert, M. Reis, A. Au, R. Cowan, and R. C. Dowell, *Cochlear implantation outcomes in adults: A scoping review*, PLoS One **15**, e0232421 (2020), type: Journal Article.
- [3] M. Hariz and P. Blomstedt, *Deep brain stimulation for Parkinson's disease*, J Intern Med **292**, 764 (2022), type: Journal Article.
- [4] M. Hodaie, R. A. Wennberg, J. O. Dostrovsky, and A. M. Lozano, *Chronic anterior thalamus stimulation for intractable epilepsy*, Epilepsia **43**, 603 (2002), type: Journal Article.
- [5] T. J. Foutz and M. Wong, *Brain stimulation treatments in epilepsy: Basic mechanisms and clinical advances*, Biomed J **45**, 27 (2022), type: Journal Article.
- [6] T. J. Oxley, P. E. Yoo, G. S. Rind, S. M. Ronayne, C. M. S. Lee, C. Bird, V. Hampshire, R. P. Sharma, A. Morokoff, D. L. Williams, C. MacIsaac, M. E. Howard, L. Irving, I. Vrljic, C. Williams, S. E. John, F. Weissenborn, M. Dzenko, A. H. Balabanski, D. Friedenberg, A. N. Burkitt, Y. T. Wong, K. J. Drummond, P. Desmond, D. Weber, T. Denison, L. R. Hochberg, S. Mathers, T. J. O'Brien, C. N. May, J. Mocco, D. B. Grayden, B. C. V. Campbell, P. Mitchell, and N. L. Opie, *Motor neuroprosthesis implanted with neurointerventional surgery improves capacity for activities of daily living tasks in severe paralysis: first in-human experience*, Journal of NeuroInterventional Surgery **13**, 102 (2021), publisher: British Medical Journal Publishing Group.

- [7] M. Hughes, K. Bustamante, D. Banks, and D. Ewins, *Effects of electrode size on the performance of neural recording microelectrodes*, in *1st Annual International IEEE-EMBS Special Topic Conference on Microtechnologies in Medicine and Biology. Proceedings (Cat. No.00EX451)* (2000) pp. 220–223.
- [8] R. Hu, P. Fan, Y. Wang, J. Shan, L. Jing, W. Xu, F. Mo, M. Wang, Y. Luo, Y. Wang, X. Cai, and J. Luo, *Multi-channel microelectrode arrays for detection of single-cell level neural information in the hippocampus CA1 under general anesthesia induced by low-dose isoflurane*, Fundamental Research <https://doi.org/10.1016/j.fmre.2023.05.015> (2023).
- [9] A. I. Kashkoush, R. A. Gaunt, L. E. Fisher, T. M. Bruns, and D. J. Weber, *Recording single- and multi-unit neuronal action potentials from the surface of the dorsal root ganglion*, Scientific Reports **9**, 2786 (2019), type: Journal Article.
- [10] J. Jiang, F. R. Willett, and D. M. Taylor, *Relationship between microelectrode array impedance and chronic recording quality of single units and local field potentials*, in *2014 36th Annual International Conference of the IEEE Engineering in Medicine and Biology Society* (2014) pp. 3045–3048.
- [11] P. R. Patel, K. Na, H. Zhang, T. D. Y. Kozai, N. A. Kotov, E. Yoon, and C. A. Chestek, *Insertion of linear 8.4  $\mu\text{m}$  diameter 16 channel carbon fiber electrode arrays for single unit recordings*, Journal of Neural Engineering **12**, 046009 (2015), publisher: IOP Publishing.
- [12] B. Neurotech, *Utah Array* (2024).
- [13] K. Woeppel, C. Hughes, A. J. Herrera, J. R. Eles, E. C. Tyler-Kabara, R. A. Gaunt, J. L. Collinger, and X. T. Cui, *Explant Analysis of Utah Electrode Arrays Implanted in Human Cortex for Brain-Computer-Interfaces*, Frontiers in Bioengineering and Biotechnology **9**, 10.3389/fbioe.2021.759711 (2021).
- [14] P. A. Cody, J. R. Eles, C. F. Lagenaur, T. D. Y. Kozai, and X. T. Cui, *Unique electrophysiological and impedance signatures between encapsulation types: An analysis of biological Utah array failure and benefit of a biomimetic coating in a rat model*, Biomaterials **161**, 117 (2018).
- [15] G. Baranauskas, E. Maggiolini, E. Castagnola, A. Ansaldi, A. Mazzoni, G. N. Angotzi, A. Vato, D. Ricci, S. Panzeri, and L. Fadiga, *Carbon nanotube composite coating of neural microelectrodes preferentially improves the multiunit signal-to-noise ratio*, Journal of Neural Engineering **8**, 066013 (2011).
- [16] M. Hejazi, W. Tong, M. R. Ibbotson, S. Prawer, and D. J. Garrett, *Advances in Carbon-Based Microfiber Electrodes for Neural Interfacing*, Frontiers in Neuroscience **15**, 658703 (2021).
- [17] T. L. Massey, S. R. Santacruz, J. F. Hou, K. S. J. Pister, J. M. Carmena, and M. M. Marnabiz, *A high-density carbon fiber neural recording array technology*, Journal of Neural Engineering **16**, 016024 (2019), publisher: IOP Publishing.

- [18] M. A. Hejazi, W. Tong, A. Stacey, A. Soto-Breceda, M. R. Ibbotson, M. Yunzab, M. I. Maturana, A. Almasi, Y. J. Jung, S. Sun, H. Meffin, J. Fang, M. E. M. Stamp, K. Ganesan, K. Fox, A. Rifai, A. Nadarajah, S. Falahatdoost, S. Prawer, N. V. Apollo, and D. J. Garrett, *Hybrid diamond/ carbon fiber microelectrodes enable multimodal electrical/chemical neural interfacing*, *Biomaterials* **230**, 119648 (2020).
- [19] J. Richie, *Exploration and Realization of Sub-Neuronal Carbon Fiber Electrodes for Recording and Stimulation in the Nervous System*, PhD Thesis, The University of Michigan (2024).
- [20] S.-J. Kim, S. C. Manyam, D. J. Warren, and R. A. Normann, *Electrophysiological Mapping of Cat Primary Auditory Cortex with Multielectrode Arrays*, *Annals of Biomedical Engineering* **34**, 300 (2006).
- [21] Steven Prawer, David Garrett, *High-resolution neural implants for epilepsy treatment*.
- [22] M. Golda-Cepa, K. Engvall, M. Hakkarainen, and A. Kotarba, *Recent progress on parylene C polymer for biomedical applications: A review*, *Progress in Organic Coatings* **140**, 105493 (2020).
- [23] J. P. Neto, P. Baiao, G. Lopes, J. Frazao, J. Nogueira, E. Fortunato, P. Barquinha, and A. R. Kampff, *Does Impedance Matter When Recording Spikes With Polytrodes?*, *Frontiers in Neuroscience* **12**, 10.3389/fnins.2018.00715 (2018).
- [24] C. M. Lewis, C. Boehler, R. Liljemalm, P. Fries, T. Stieglitz, and M. Asplund, *Recording Quality Is Systematically Related to Electrode Impedance*, *Advanced Healthcare Materials* **13**, 2303401 (2024).
- [25] A. R. Harris, C. Newbold, D. Stathopoulos, P. Carter, R. Cowan, and G. G. Wallace, *Comparison of the In Vitro and In Vivo Electrochemical Performance of Bionic Electrodes*, *Micromachines* **13**, 10.3390/mi13010103 (2022).
- [26] A. R. Harris, B. J. Allitt, and A. G. Paolini, *Predicting neural recording performance of implantable electrodes*, *Analyst* **144**, 2973 (2019), publisher: The Royal Society of Chemistry.
- [27] T. Chung, J. Q. Wang, J. Wang, B. Cao, Y. Li, and S. W. Pang, *Electrode modifications to lower electrode impedance and improve neural signal recording sensitivity*, *Journal of Neural Engineering* **12**, 056018 (2015), publisher: IOP Publishing.
- [28] Y. J. Jung, A. Almasi, S. H. Sun, M. Yunzab, S. L. Cloherty, S. H. Bauquier, M. Renfree, H. Meffin, and M. R. Ibbotson, *Orientation pinwheels in primary visual cortex of a highly visual marsupial*, *Science Advances* **8**, eabn0954 (2022), publisher: American Association for the Advancement of Science.
- [29] Y. J. Jung, A. Almasi, S. Sun, M. Yunzab, S. H. Baquier, M. Renfree, H. Meffin, and M. R. Ibbotson, *Feature selectivity and invariance in marsupial primary visual cortex*, *The Journal of Physiology* **603**, 423 (2025).

- [30] H. Cui, X. Xie, S. Xu, L. L. H. Chan, and Y. Hu, *Electrochemical characteristics of microelectrode designed for electrical stimulation*, BioMedical Engineering OnLine **18**, 86 (2019).
- [31] S. F. Cogan, J. Ehrlich, and T. D. Plante, *The effect of electrode geometry on electrochemical properties measured in saline*, in *2014 36th Annual International Conference of the IEEE Engineering in Medicine and Biology Society* (2014) pp. 6850–6853.
- [32] K. Kansara and A. Kumar, *In vitro methods to assess the cellular toxicity of nanoparticles*, in *Nanotoxicity, Micro and Nano Technologies* (Elsevier, 2020) pp. 21–40.
- [33] Gamry Instruments, *Two, Three, Four Electrode System Gamry 4-Probe Potentiostats Gamry Instruments* (2025).
- [34] K. Shen, O. Chen, J. L. Edmunds, D. K. Piech, and M. M. Maharbiz, *Translational opportunities and challenges of invasive electrodes for neural interfaces*, Nature Biomedical Engineering **7**, 424 (2023).
- [35] S. Wang, J. Zhang, O. Gharbi, V. Vivier, M. Gao, and M. E. Orazem, *Electrochemical impedance spectroscopy*, Nature Reviews Methods Primers **1**, 1 (2021), publisher: Nature Publishing Group.
- [36] A. C. Lazanas and M. I. Prodromidis, *Electrochemical Impedance Spectroscopy-A Tutorial*, ACS Measurement Science Au **3**, 162 (2023).
- [37] S. M. Gateman, O. Gharbi, H. Gomes De Melo, K. Ngo, M. Turmine, and V. Vivier, *On the use of a constant phase element (CPE) in electrochemistry*, Current Opinion in Electrochemistry **36**, 101133 (2022).
- [38] G. Brug, A. Van Den Eeden, M. Sluyters-Rehbach, and J. Sluyters, *The analysis of electrode impedances complicated by the presence of a constant phase element*, Journal of Electroanalytical Chemistry and Interfacial Electrochemistry **176**, 275 (1984).
- [39] V. Viswam, M. E. J. Obien, F. Franke, U. Frey, and A. Hierlemann, *Optimal Electrode Size for Multi-Scale Extracellular-Potential Recording From Neuronal Assemblies*, Frontiers in Neuroscience **13**, 10.3389/fnins.2019.00385 (2019), publisher: Frontiers.
- [40] A. Susloparova, S. Halliez, S. Begard, M. Colin, L. Buee, S. Pecqueur, F. Alibart, V. Thomy, S. Arscott, E. Pallecchi, and Y. Coffinier, *Low impedance and highly transparent microelectrode arrays (MEA) for in vitro neuron electrical activity probing*, Sensors and Actuators B: Chemical **327**, 128895 (2021).
- [41] P. D. Jones, A. Moskalyuk, C. Barthold, K. Gutohrlein, G. Heusel, B. Schroppel, R. Samba, and M. Giugliano, *Low-Impedance 3D PEDOT:PSS Ultramicroelectrodes*, Frontiers in Neuroscience **14**, 10.3389/fnins.2020.00405 (2020).
- [42] P. Wilson, *Chapter 1 - Grounding and Wiring*, in *The Circuit Designer's Companion (Fourth Edition)*, edited by P. Wilson (Newnes, 2017) pp. 1–47.

- [43] J. Gunderson, *Manuals & Documentation - Ripple Neuro* ↗ [riplleneuro.com](http://riplleneuro.com) (2021).
- [44] R. C. Kelly, M. A. Smith, J. M. Samonds, A. Kohn, A. B. Bonds, J. A. Movshon, and T. S. Lee, *Comparison of Recordings from Microelectrode Arrays and Single Electrodes in the Visual Cortex*, Journal of Neuroscience **27**, 261 (2007), publisher: Society for Neuroscience Section: Toolbox.
- [45] J. Stedehouder, D. Verdier, A. Kolta, and S. J. Cragg, *Making Ca<sup>2+</sup> - selective microelectrodes* (2024).
- [46] *Potentiostat Stability: Tips for Improving Potentiostat Stability Gamry Instruments*.
- [47] K. Ludwig, J. Uram, J. Yang, D. Martin, and D. Kipke, *Chronic neural recordings using silicon microelectrode arrays electrochemically deposited with a poly(3,4-ethylenedioxythiophene) (PEDOT) film*, Journal of neural engineering **3**, 59 (2006).
- [48] Y. J. Jung, *To be announced* (2025), manuscript in preparation.
- [49] Z. Aqrawe, N. Patel, Y. Vyas, M. Bansal, J. Montgomery, J. Travas-Sejdic, and D. Svirskis, *A simultaneous optical and electrical in-vitro neuronal recording system to evaluate microelectrode performance*, PLOS ONE **15**, e0237709 (2020).
- [50] L. D. Garma, L. Matino, G. Melle, F. Moia, F. De Angelis, F. Santoro, and M. Dipalo, *Cost-effective and multifunctional acquisition system for in vitro electrophysiological investigations with multi-electrode arrays*, PLOS ONE **14**, 1 (2019), publisher: Public Library of Science.
- [51] M. Ghazal, C. Scholaert, C. Dumortier, C. Lefebvre, N. Barois, S. Janel, M. C. Tarhan, M. Colin, L. Buee, S. Halliez, S. Pecqueur, Y. Coffinier, F. Alibart, and P. Yger, *Precision of neuronal localization in 2D cell cultures by using high-performance electropolymerized microelectrode arrays correlated with optical imaging*, Biomedical Physics & Engineering Express **9**, 035016 (2023), publisher: IOP Publishing.
- [52] M. Boscherini, *Low-cost Neuronal Network Electronic Readout Circuit for Micro-Graphitic Diamond Multi-Electrode Arrays*, Master's thesis, Politecnico di Torino (2022).
- [53] M. Weigand, F. Sartori, and H. Cuntz, *Universal transition from unstructured to structured neural maps*, Proceedings of the National Academy of Sciences **114**, E4057 (2017), publisher: Proceedings of the National Academy of Sciences.
- [54] M.-E. Laramee and D. Boire, *Visual cortical areas of the mouse: comparison of parcellation and network structure with primates*, Frontiers in Neural Circuits **8**, 149 (2015).
- [55] R. Fiath, D. Meszena, Z. Somogyvari, M. Boda, P. Bartho, P. Ruther, and I. Ulbert, *Recording site placement on planar silicon-based probes affects signal quality in acute neuronal recordings*, Scientific Reports **11**, 2028 (2021).
- [56] R. Fiath, A. L. Marton, F. Matyas, D. Pinke, G. Marton, K. Toth, and I. Ulbert, *Slow insertion of silicon probes improves the quality of acute neuronal recordings*, Scientific Reports **9**, 111 (2019).

- [57] M. Y. Villeneuve and C. Casanova, *On the use of isoflurane versus halothane in the study of visual response properties of single cells in the primary visual cortex*, Journal of Neuroscience Methods **129**, 19 (2003).
- [58] M. McNamara, A. Ersoz, and M. Han, *A Diagnostic Circuit for Crosstalk Detection in Microelectrode Arrays*, in *2021 10th International IEEE/EMBS Conference on Neural Engineering (NER)* (IEEE, Italy, 2021) pp. 544–547.
- [59] N. V. Swindale and M. A. Spacek, *Verification of multichannel electrode array integrity by use of cross-channel correlations*, Journal of Neuroscience Methods **263**, 95 (2016).
- [60] V. O. Makarov and M. Trontelj, *Sintering and electrical conductivity of doped WO<sub>3</sub>*, Journal of the European Ceramic Society **16**, 791 (1996).
- [61] S. F. Cogan, *In vivo and In vitro Differences in the Charge-injection and Electrochemical Properties of Iridium Oxide Electrodes*, in *2006 International Conference of the IEEE Engineering in Medicine and Biology Society* (2006) pp. 882–885, iSSN: 1557-170X.
- [62] E. Musk and Neuralink, *An Integrated Brain-Machine Interface Platform With Thousands of Channels*, Journal of Medical Internet Research **21**, e16194 (2019).
- [63] C. HorvÁth, L. F. Toth, I. Ulbert, and R. Fiath, *Dataset of cortical activity recorded with high spatial resolution from anesthetized rats*, Scientific Data **8**, 180 (2021).
- [64] A. Almasi, S. H. Sun, Y. J. Jung, M. Ibbotson, and H. Meffin, *Data-driven modelling of visual receptive fields: comparison between the generalized quadratic model and the nonlinear input model*, Journal of Neural Engineering **21**, 046014 (2024).
- [65] A. Almasi, S. H. Sun, M. Yunzab, Y. J. Jung, H. Meffin, and M. R. Ibbotson, *How Stimulus Statistics Affect the Receptive Fields of Cells in Primary Visual Cortex*, The Journal of Neuroscience **42**, 5198 (2022).
- [66] A. J. Rockel, R. W. Hiorns, and T. P. S. Powell, *THE BASIC UNIFORMITY IN STRUCTURE OF THE NEOCORTEX*, Brain **103**, 221 (1980).
- [67] S. Srinivasan, C. N. Carlo, and C. F. Stevens, *Predicting visual acuity from the structure of visual cortex*, Proceedings of the National Academy of Sciences **112**, 7815 (2015).
- [68] A. Peters and D. A. Kara, *The neuronal composition of area 17 of rat visual cortex. I. The pyramidal cells*, Journal of Comparative Neurology **234**, 218 (1985).
- [69] C. A. Knox, *Effects of aging and chronic arterial hypertension on the cell populations in the neocortex and archicortex of the rat*, Acta Neuropathologica **56**, 139 (1982).
- [70] L. Werner, A. Wilke, R. BlÁdner, E. Winkelmann, and K. Brauer, *Topographical distribution of neuronal types in the albino rat's area 17. A qualitative and quantitative Nissl study*, Zeitschrift Fur Mikroskopisch-Anatomische Forschung **96**, 433 (1982).
- [71] P. Gabbott and M. Stewart, *Distribution of neurons and glia in the visual cortex (area 17) of the adult albino rat: A quantitative description*, Neuroscience **21**, 833 (1987).

- [72] C. Beaulieu and M. Colonnier, *The number of neurons in the different laminae of the binocular and monocular regions of area 17 in the cat*, Journal of Comparative Neurology **217**, 337 (1983).
- [73] N. A. Young, C. E. Collins, and J. H. Kaas, *Cell and neuron densities in the primary motor cortex of primates*, Frontiers in Neural Circuits **7**, 30 (2013).
- [74] D. A. Sholl, *A comparative study of the neuronal packing density in the cerebral cortex*, Journal of Anatomy **93**, 143 (1959).
- [75] G. Merkel and E. I. Eger, *A Comparative Study of Halothane and Halopropane Anesthesia: Including Method for Determining Equipotency*, Anesthesiology **24**, 346 (1963).
- [76] I. Nauhaus, A. Benucci, M. Carandini, and D. L. Ringach, *Neuronal Selectivity and Local Map Structure in Visual Cortex*, Neuron **57**, 673 (2008).

## Appendices

### A Supplementary Figures

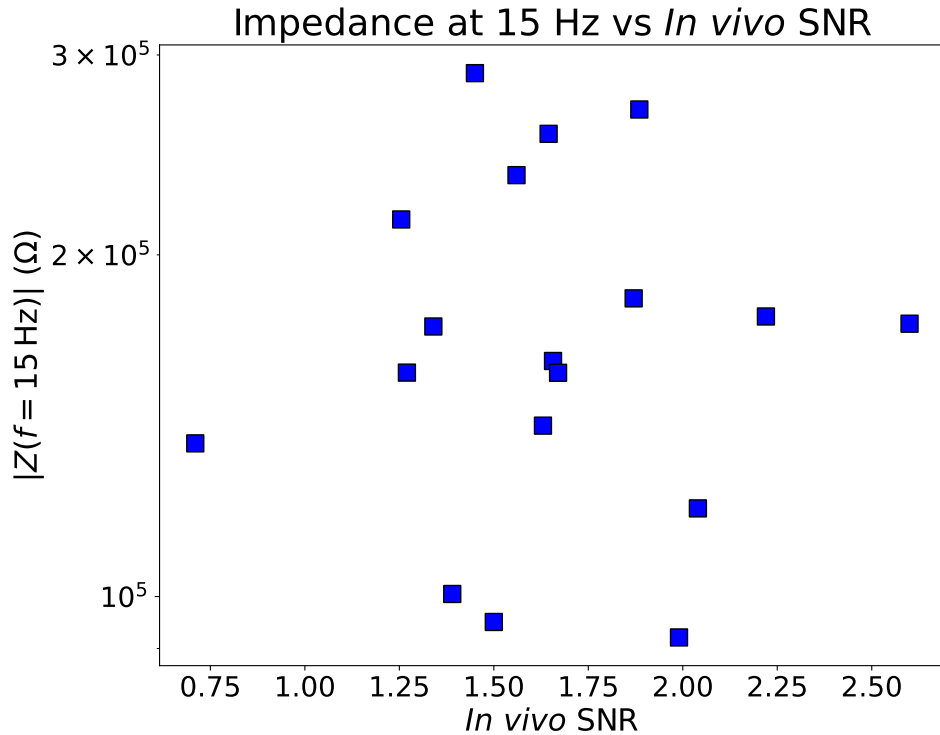


Figure A1. Plot of 15 Hz impedance magnitude versus *in vivo* SNR. No clear trend was observed, consistent with 1 kHz results.

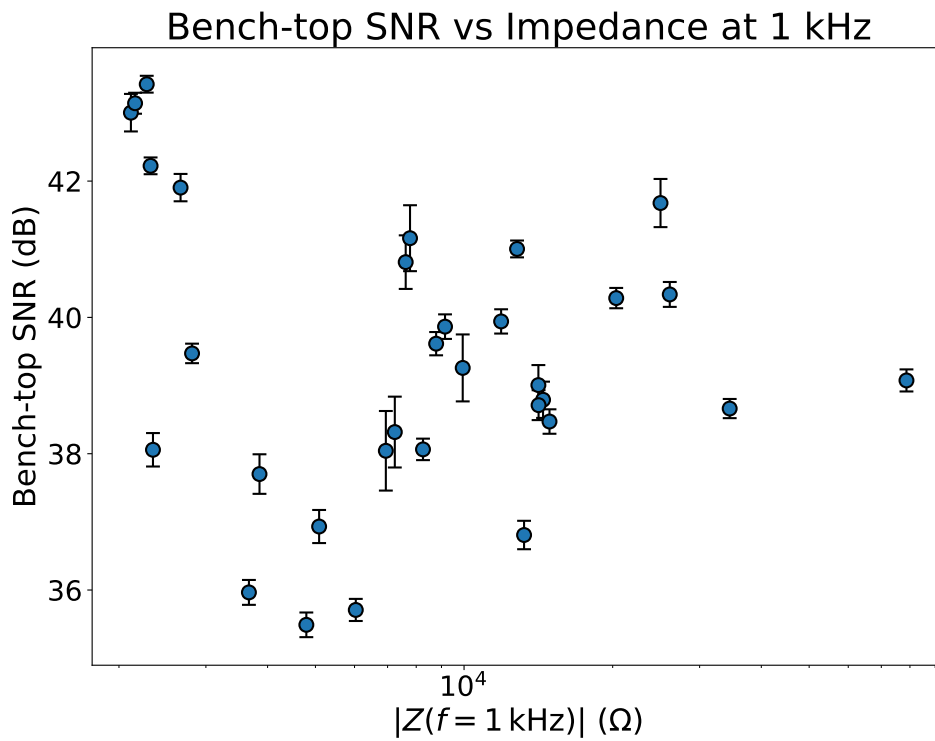


Figure A2. Relationship between bench-top SNR and impedance magnitude at 1 kHz for CC MEAs. No significant monotonic relationship was observed between impedance and bench-top SNR (Spearman  $\rho = -0.104$ ,  $p = 0.572$ ). However, Levene's test indicated a significant difference in SNR variance across impedance values ( $W = 13.253$ ,  $p = 0.001$ ). This suggests that while impedance magnitude does not have a clear relationship with SNR, the consistency of bench-top recording quality varies with impedance. Specifically, certain impedance ranges exhibit greater variability in SNR. Error bars represent the standard deviation of the SNR across repeated responses to a biphasic waveform.

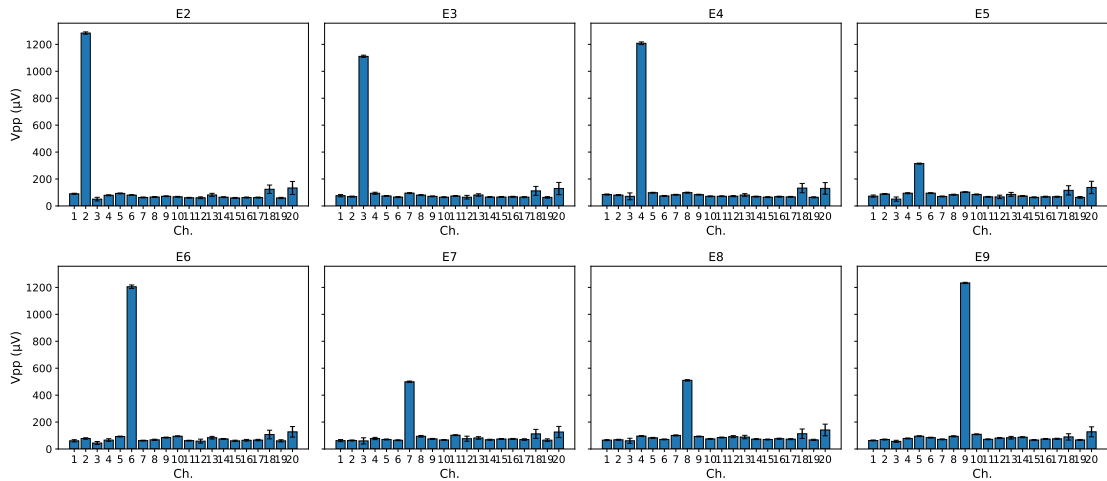


Figure A3. Bar plots of the average peak-to-peak voltage ( $V_{PP}$ ) across all 20 channels during stimulation of a sample of electrodes (E2-E9). The variation in recorded magnitude on the stimulated channel is due to differing separation between the patch-clamp electrode and the carbon-fibre channel.